Energy Conversion and Management 199 (2019) 111924

Contents lists available at ScienceDirect

Energy Conversion and Management

journal homepage: www.elsevier.com/locate/enconman

Model-based predictive control for optimal MicroCSP operation integrated with building HVAC systems

Mohamed Toub[a,*], Chethan R. Reddy[b], Meysam Razmara[b], Mahdi Shahbakhti[b], Rush D. Robinett III[b], Ghassane Aniba[a]

[a] Mohammadia School of Engineering, Mohammed V University of Rabat, Rabat 10080, Morocco
[b] Mechanical Engineering Department, Michigan Technological University, Houghton, MI 49931, USA

ARTICLE INFO

Keywords:
Building energy management
Model predictive control
MicroCSP
Solar energy conversion
HVAC system optimization

ABSTRACT

This paper presents a model predictive control (MPC) framework to minimize the energy consumption and the energy cost of the building heating, ventilation, and air-conditioning (HVAC) system integrated with a micro-scale concentrated solar power (MicroCSP) system that cogenerates electricity and heat. The mathematical model of a MicroCSP system is derived and integrated into the building thermal model of an office building at Michigan Technological University. Then, the MPC framework is used to optimize thermal energy storage (TES) system usage, the energy conversion in the Organic Rankine Cycle (ORC), and the thermal energy flows to the HVAC system. The MPC results for energy and cost savings show the significance of understanding system dynamics and designing a real-time predictive controller to maximize the benefits of MicroCSP thermal and electrical energies production. Indeed, the designed MPC framework provided 37% energy saving and 70% cost saving compared to the conventional rule-based controller (RBC). Furthermore, the MicroCSP integration into the building HVAC is compared to the alternative of integrating photovoltaic (PV) panels and battery energy storage (BES) system to address the building HVAC needs. The results show the MicroCSP system outperforms PV solar panels for energy saving, while the PV panels outperform the MicroCSP system for cost saving when dynamic pricing is applied.

1. Introduction

Two of the main challenges facing the world in the 21st century are the fossil fuels scarcity and the greenhouse gas (GHG) emissions. These require considerable efforts to reduce the GHG negative impacts on the environment, take preventive measures against climate change, and preserve the natural resources so that they can continue to be sustainably exploited [1].

The U.S. Environmental Protection Agency (EPA) reported that electricity production contributed to 36% of the total CO2 emissions in the U.S. in 2016 [2]. In addition, the commercial and residential buildings were responsible for 74% of the U.S. electricity consumption in 2017 [3], while a third of this consumption was imputed to the heating, ventilation, and air-conditioning (HVAC) systems [4]. Therefore, due to their energy-intensive nature and the associated GHG emissions, HVAC systems are important parts of the energy efficiency programs in the U.S.

Solar energy is one of the largest potential sources of renewable energy. It is suggested that the entire world yearly energy needs can be fulfilled by covering only 0.1% of the surface of the earth by solar collectors with merely 20% efficiency [5]. Moreover, solar energy can be a cost-effective and sustainable alternative to grid-extension and fuel-based electricity generation for rural electrification especially in Africa which has a low electrification rate while possessing an important solar potential [6]. The two main technologies that use solar energy are (i) the well-known photovoltaic (PV) technology which is mainly used to produce electricity and (ii) the concentrated solar power (CSP) technology that produces both electrical and thermal energy.

The U.S. Department of Energy (DOE) launched in 2011 the SunShot Initiative that aims to make solar energy more competitive by reducing the cost of the utility-scale installations by 75% bringing it to around $1 per Watt [7]. More recently, in 2018, the DOE awarded $72 million for projects dedicated to developing the next generation of advanced CSP systems [8].

Although high-temperature CSP technology is well developed for large power plants and in use for years, micro-scale concentrated solar

* Corresponding author.
E-mail addresses: mohamedtoub@research.emi.ac.ma (M. Toub), creddy@mtu.edu (C.R. Reddy), mrazmara@mtu.edu (M. Razmara), mahdish@mtu.edu (M. Shahbakhti), rdrobine@mtu.edu (R.D. Robinett), ghassane@emi.ac.ma (G. Aniba).

https://doi.org/10.1016/j.enconman.2019.111924
Received 25 May 2019; Received in revised form 5 August 2019; Accepted 6 August 2019
Available online 06 September 2019
0196-8904/

Nomenclature

Abbreviations

AHU	air handling unit
BES	battery energy storage
COP	coefficient of performance
CSP	concentrated solar power
DNI	direct normal irradiance
ERV	energy recovery ventilator
ETC	evacuated tube collectors
FLT	first law of thermodynamics
HP	heat pump
HTF	heat transfer fluid
HVAC	heating, ventilation, and air conditioning
LMP	locational marginal price
MicroCSP	micro-scale CSP
MPC	model predictive control
ORC	organic rankine cycle
PTC	parabolic trough collectors
PV	photovoltaic
RBC	rule based control
SOC	state of charge
TES	thermal energy storage
WF	working fluid

Symbols

θ	incidence angle (rad)
θ_Z	zenith angle (rad)
T_{solar}	solar time (h)
$T_{standard}$	standard time (h)
DST	daylight saving time (h)
L_{st}	meridian of local time zone (–)
L_{loc}	meridian of collector site (–)
E_t	equation of time (h)
β	Fractional year (rad)
ϕ	latitude angle (rad)
δ	declination angle (rad)
ω	hour angle (rad)
n	day number starting from January 1st (–)
η_0	optical efficiency of collectors (–)
IAM	incidence angle modifier (rad)
A_p	aperture area (m^2)
DNI	direct normal irradiance (W/m^2)
T_{htf}	HTF average temperature (K)
T_{amb}	ambient temperature (K)
$T_{htf,in}$	PTC solar array inlet temperature (K)
$T_{htf,out}$	PTC solar array outlet temperature (K)
$c_{p,air}$	specific heat of the air (J/(kg.K))
COP	coefficient of performance of the HP (–)
$\mathscr{T}^{su}$	supply air temperature to thermal zone (K)
T^{HP}	supply air temperature to the HP (K)
T^{ERV}	ERV outlet air temperature (K)
$\bar{\mathscr{T}}$	supply air temperature limit (K)
$\overline{T^r}$	thermal zone temperature upper bound (K)
$\underline{T^r}$	thermal zone temperature lower bound (K)
$\dot{Q}_{abs}$	absorbed solar power (W)
$\dot{Q}_{loss}$	heat loss in collectors (W)
$\dot{m}_{htf}$	HTF mass flow rate in the collectors (kg/s)
P_e	recirculator power consumption (W)
P_{htf}	power required for HTF recirculation (W)
η_{recir}	recirculator efficiency (–)
Δp	pressure drop (Pa)
ρ_{htf}	HTF density (kg/m^3)
$\dot{Q}_{SOL}$	thermal power produced by the PTC solar array (W)
h_x	WF specific enthalpy at state x (J/kg)
η_{gen}	efficiency of the ORC turbine generator (–)
η_{motor}	efficiency of the ORC pump motor (–)
$\dot{m}_{wf}$	mass flow rate of the WF (kg/s)
P_{gross}	ORC gross electrical power (W)
P_{pump}	ORC pump motor power (W)
P_{ORC}	ORC net electrical power (W)
$\dot{Q}_{COG}$	ORC cogeneration heat flow rate (W)
$\dot{Q}_{TES}$	heat flow rate from TES to ORC (W)
C_{TES}	capacity of the TES (Wh)
$\dot{m}_{tes}$	HTF mass flow rate from TES (kg/s)
$c_{p,htf}$	specific heat of the HTF (J/(kg.K))
$T_{ev,in}$	ORC evaporator inlet temperature (K)
$T_{ev,out}$	ORC evaporator outlet temperature (K)
r_p	pressure ratio of the WF (–)
I_e	building HVAC energy consumption (W)
λ_F	HVAC fan power coefficient ($W.\ s^3/kg^3$)
$\dot{m}^r$	supply air mass flow rate (kg/s)
N	prediction horizon (–)
P_{PV}	electricity power produced by the PV solar array (W)
P_{S2B}	power from the BES to the building (W)
P^F	ventilation fan power consumption (W)
P^H	HP power consumption (W)
t	current time (s)
t_f	final time (s)
N_z	number of zones in the building (–)
$\dot{m}^{su}$	mass flow rate of the supply air (kg/s)
$\dot{m}^v$	fresh air mass flow rate to thermal zones (kg/s)
T^z	thermal zone temperature (K)
ERE	energy recovery ventilator effectiveness (–)
P_{Grid}	power from grid to building (W)
ρ	weight of soft constraints (–)
$\overline{SOC}$	SOC upper bound (%)
$\underline{SOC}$	SOC lower bound (%)
$\dot{m}_{max}$	ORC evaporator mass flow limit (kg/s)
$\underline{\epsilon}_t$	optimization lower slack variable (K)
$\bar{\epsilon}_t$	optimization upper slack variable (K)
C_{BES}	capacity of the BES (Ah) (W)
V_B	voltage across the battery (V)

power (MicroCSP) systems, with less than 1 MW of rated power, did not become popular until recent years [9]. The well-known Organic Rankine cycle (ORC) technology is used in MicroCSP to mimic the conventional Ranking cycle by using an organic fluid instead of water to convert low-grade thermal energy into electrical energy [10]. Despite its inherent low thermal efficiency, the ORC engine can increase the overall efficiency of a building system by providing low-grade waste heat to the low-temperature thermal loads [11]. Furthermore, optimally designed ORC engines coupled with solar collectors, such as flat-plate collectors or evacuated tube collectors, have a great potential for domestic applications and present a levelized cost of energy comparable to PV systems [12]. This work falls within the context of a research project that aims to develop an optimal control framework to analyze the potential of MicroCSP technology to exploit its low-grade heat cogeneration for building applications. The MicroCSP includes a thermal energy storage (TES) system to improve system performance when solar energy is unavailable.

Integration of solar energy in buildings HVAC systems to reduce energy consumption and energy cost is well reported in the literature. Authors in references [13,14] built a solar-thermal-assisted HVAC

system. They used flat-panel and vacuum tube solar collectors to produce heat and store it in a TES system before using it to provide either heating through a heat exchanger, or cooling through an absorption chiller to a university campus building. Using look-ahead scheduling, the authors in [13,14] achieved a 30% annual cost saving by considering day-ahead irradiation and temperature forecasts [15]. A hybrid solar-assisted HVAC and water heating system was presented in reference [16]. The authors used a rolling stochastic optimization method for the smart scheduling of energy and showed a substantial reduction of the energy cost. Authors in reference [17] investigated the coupling of PV-thermal collectors to HP and absorption chillers. Simulations were performed for ten locations in Europe with different configurations. The results show that the combined system can cover up to 60% of the heating load and almost 100% of the cooling demand. In another paper, authors in reference [18] carried out an economic analysis of PV-thermal collectors for building integration in Sweden for heat and power cogeneration. Using Monte Carlo simulations, the sensitivity analysis on 11 factors showed that PV-thermal collectors are more profitable for locations with high solar irradiance and high heating prices. In reference [19], the authors presented a combined trigeneration solar system based on PV-thermal collectors coupled with absorption chillers. Using measurement data from a university campus testbed, an economic analysis was performed to compare the PV-thermal-based system with both the conventional PV-based system and evacuated tube collectors (ETC)-based system. The results show that the PV-thermal-based system has 2.7 times higher payback time compared to PV-based system and 2.3 times shorter payback time than the ETC-based system. Besides, the PV-thermal-based system presents a significant reduction in GHG emissions. In reference [20], several hybrid systems including PV/micro-CHP/solar thermal integrated into a building were simulated to investigate their potential in reducing the emissions and energy consumption. Authors in reference [21] considered flat-plate evacuated solar collectors for a small-scale combined cooling, heating, and power trigeneration system used in building applications. The performance analysis showed that optimal selection of the design parameters, such as the storage size, can improve the overall efficiency by 6.5%. The aforementioned studies focused only on the benefits of combining solar energy with different systems for building heating and cooling; however, they did not address the control challenges for optimal operation of these combined solar energy integrated systems.

The stochastic nature of the solar irradiation and its limitation to the daylight hours make the control of solar energy integrated into buildings very challenging. However, TES can be interfaced with solar energy to make it more dispatchable. The relative simplicity of TES for high dispatchability gives the CSP technology a competitive advantage over PV [22]. Hence, TES system has been integrated into CSP plants to act as a buffer for storing heat and delivering it on-demand; thus, improving the dispatchability of solar power and encouraging renewable energy integration in power plants [23]. For utility-scale CSP plants, over 97% round-trip efficiencies were reported in reference [24] with two-tanks TES systems and molten solar salt. For a 1 MW CSP system, authors in reference [25] showed that notwithstanding solar energy variations, the two-tank TES system can guarantee a constant power output and increase the penetration rate of solar energy by as much as 47% and up to 70% on sunny days. Furthermore, several advanced control techniques have been applied to CSP systems to handle the stochastic nature of solar energy [26,27]. MPC is one of the most used techniques for control of solar systems. Indeed, MPC has been successfully utilized for optimal control of a building integrating heat pumps (HP) [28] with PV panels and battery energy storage (BES) [29]. Authors in reference [30] presented a hierarchical MPC for a building energy management system. They developed a modular coordination approach of MPC controllers for microgrid energy flows and building thermal comfort, and were able to minimize the operation cost of the building. In reference [31], the authors presented a hybrid MPC strategy to control solar-assisted HVAC. The air-based PV-thermal system, the phase change active storage, and the residential building HVAC system were optimally controlled in [31] to achieve efficiency and thermal comfort objectives.

This study considers a MicroCSP plant integrated into the HVAC system of an office building. Solar energy captured by the parabolic trough collectors (PTC) is converted into thermal energy. This thermal energy is stored in a TES system and dispatched to the ORC to cogenerate both electrical and low-grade thermal power when needed. The low-grade heat preheats the fresh air coming from the Energy Recovery Ventilator (ERV) system and/or the recycled air from the rooms in the building, while the electricity production contributes to the reduction of the electrical energy consumption from the power grid.

For optimal usage of energy from MicroCSP, the TES system must store the thermal energy from PTC solar array and dispatch it to the ORC according to the building HVAC needs. Hence, in this study, an MPC is designed to optimally control TES usage along with the thermal energy flows from the HP to the building. The MPC can provide a real-time optimal solution, deciding whether to use solar energy to supply cogenerated heat to the rooms in the building by dispatching thermal energy from the TES to the ORC or to use electrical energy from the grid to run the HP to heat the rooms. Additionally, by controlling the indoor temperature based on the solar irradiation forecast and the current and future desired temperature set points, MPC can guarantee thermal comfort while handling constraints on the operating limits of the HP, the ORC, and the state of charge (SOC) of the TES.

To the best of authors' knowledge, this paper is the *first study* undertaken to design an optimal model-based predictive controller to maximize energy and cost savings from a building HVAC system integrated with a MicroCSP system. It also presents the first study to compare MPC results of energy and cost saving, using MicroCSP along with HVAC system, with using PV panels combined with the HVAC system.

This paper builds upon our prior works in [32,33] and proposes a new real-time model-based predictive controller for both energy saving and electricity cost saving of a building integrating a MicroCSP system with an optimally sized TES system. To assess its performance, the MicroCSP results are also compared to those of the PV. In addition, a large number of Monte Carlo Simulations are conducted to evaluate the sensitivity of reported results to i) model uncertainty, ii) seasonal weather changes, and iii) solar irradiation variations and uncertainty in predictions. The results are presented for a real test setup including an office building at Michigan Technological University and a recently purchased MicroCSP system. The building model, HVAC model, and PV panel model are experimentally validated, using experimental data, in our previous studies [34,35] and the MicroCSP model is validated using the manufacturer data [36].

The organization of the remainder of the paper is as follows. Section 2 details the building testbed. Then, the mathematical models of the PTC, TES, ORC, and the building testbed are described in Section 3. The design of the MPC framework and the formulation of the optimization problem are explained in Section 4. Next, the results of the building predictive control with MPC are presented in Section 5 and compared to the building HVAC rule-based control. This section also presents Monte Carlo simulation results to assess the effect of prediction uncertainties on building energy and cost savings using solar energy. Section 6 concludes the paper by including the major findings from this paper.

2. Experimental testbed

The Lakeshore Center building at Michigan Technological University is the building testbed considered in this study. It is an office building with three floors of 5700 m^2 area each. An individual thermal zone is composed of an office room heated by an individual HP with a nominal coefficient of performance (COP) of 3.2. The HP systems use ground source water which remains almost at a constant temperature.

Table 1
Specifications of the testbed components.

Component	Parameter	Value	Manufacturer
PTC	Aperture area	54 m^2	Soltigua PTM × 24
	Number of rows	3	
TES	HTF	Therminol VP-1	Azolis Direct two-tank
	Working temperatures	140 °C–180 °C	
	Storage volume	5 m^3	
ORC	WF	R245fa	ENOGIA
PV	Cells type	Polycrystalline	ENO-10LT
	Number of panels	108	
BES	Type	Lithium-ion	LG Chem
	Nominal capacity	5 kWh	
Inverters	CEC efficiency	96%	SolarBridge

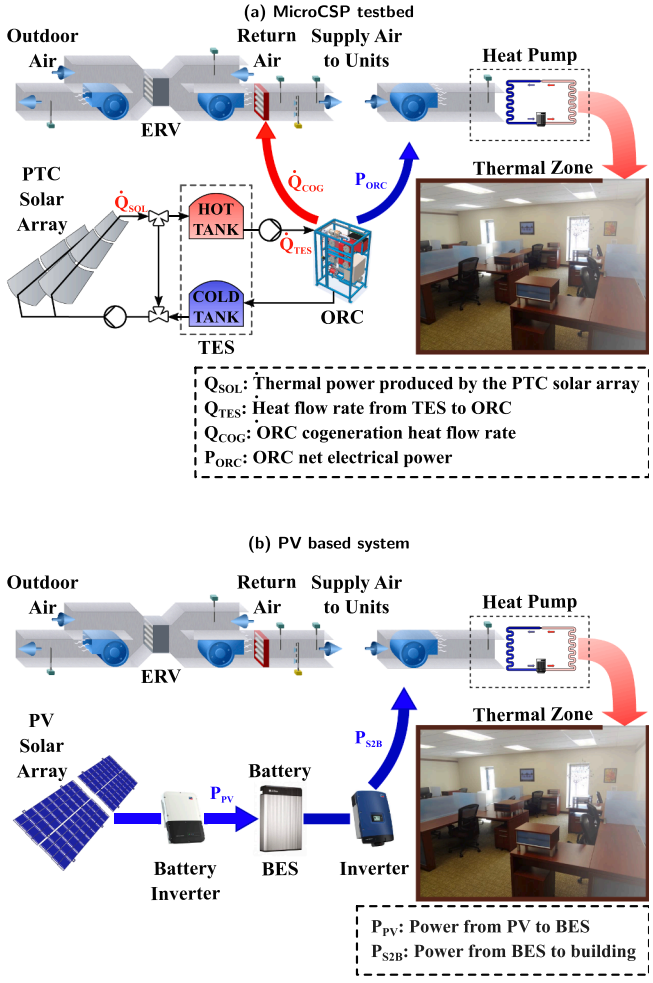

Fig. 1. Building HVAC energy flows in the MicroCSP testbed and the PV based system.

The airflow rate of the HP is also constant. Since the thermal zone air temperature is maintained within a ± 2 °C range inside the comfort zone, the assumption of constant COP is utilized in this work. The thermal zones are equipped with a temperature sensor that records the temperature data with ± 0.2 °C accuracy at a 1-min sampling rate. The building is coupled with MicroCSP and PV systems for the purpose of this study. The specifications of the MicroCSP and PV testbed components are shown in Table 1. These components are based on our existing equipment.

The experimental testbed setup in this paper is shown in Fig. 1(a). The temperature of each thermal zone is controlled by adjusting the temperature of the air supplied by the associated HP. The mass flow rate of the supply air is adjusted as proportional to the thermal zone area. The HP is supplied with air from the air handling unit (AHU). When the building is unoccupied, the returning air from the thermal zones is totally recirculated to the AHU where it can be heated by the cogeneration heat ($\dot{Q}_{COG}$) from the ORC, if available. When the building is occupied, the ERV mixes the outdoor fresh air with the returning air from the thermal zones and the resulting mixed air is heated by the cogeneration heat ($\dot{Q}_{COG}$) from the ORC, if available.

The MicroCSP system supplies low-grade cogenerated heat to the thermal zones and electricity to the HP. The thermal energy produced by the PTC solar array ($\dot{Q}_{SOL}$) is stored in the TES system. When thermal and electrical energies are needed by the building, the TES dispatches part of the stored thermal energy ($\dot{Q}_{TES}$) to run the ORC at its maximum efficiency and cogenerate electrical power (P_{ORC}) that is delivered to the building HP and thermal power ($\dot{Q}_{COG}$) that is used to preheat the building HP inlet air. The MicroCSP model is based on our recently purchased system.

In this study, the integrated MicroCSP system is compared to the PV based system, where the PV panels produce energy (P_{PV}) that is directly stored in the BES through charging inverters. Part of this stored energy (P_{S2B}) is dispatched to the building HVAC system after being converted by another inverter, as shown in Fig. 1(b).

3. Modeling

3.1. PTC model

Solar collectors are the key components for solar integration into buildings [37]. The PTC solar array considered in this study is composed of three rows of PTC, model "PTMx-24" manufactured by Soltigua [38]. Since the PTC use only direct-beam solar irradiance, each PTC row is equipped with a north-south axis tracking system allowing sun tracking from east to west. Based on astronomical formulas, optical modeling of the PTC is performed.

The incidence angle θ is the angle formed by the line perpendicular to the tracking plane and the solar beam, as shown in Fig. 2. It is related to the hour angle (ω), the declination angle (δ), and the zenith angle (θ_z) by the following equation [39]:

$$\cos(\theta) = \sqrt{\cos^2(\delta).\sin^2(\omega) + \cos^2(\theta_z)} \quad (1)$$

The hour angle ω is the angle between the local meridian and the sun such that

$$\omega = \left(T_{Solar} - 12\right).\frac{2\pi}{24} \quad (2)$$

where, T_{Solar} is the solar time which is related to the standard time

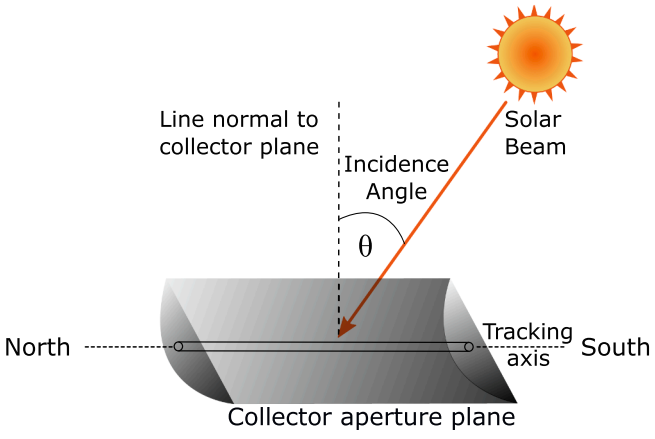

Fig. 2. Schematic of a PTC, showing the incidence angle (θ).

($T_{Standard}$) by the following equation

$$T_{Solar} = T_{Standard} - DST + \frac{L_{st} - L_{loc}}{15} + \frac{E_t}{60} \quad (3)$$

where, DST is the Daylight Saving Time which is equal to "1" during daylight-saving time otherwise it is "0". In addition, L_{loc} and L_{st} are the meridians for the collector site and the local time zone, respectively. To account for the elliptical shape of the earth's orbit, a parameter E_t known as the equation of time is used [40]:

$$E_t = 229.18 \times (0.000075 + 0.001868 \times \cos(\beta) - 0.032077 \times \sin(\beta) - 0.014615 \times \cos(2\beta) - 0.040849 \times \sin(2\beta)) \quad (4)$$

where, β is the fractional year that translates the day of the year to an angle of rotation of the earth around the sun:

$$\beta = \frac{(n-1)}{365}.\ 2\pi \quad (5)$$

where, n is the day number starting from January 1st. The declination angle δ, which is the angle between the position of the sun at noon, and the plane of the equator, varies seasonally from $-23.45\frac{\pi}{180}$ at the winter solstice to $23.45\frac{\pi}{180}$ at the summer solstice as follows [41]:

$$\delta = 23.45 \times \frac{\pi}{180} \times \sin\left(\frac{281 + n}{365} \times 2\pi\right) \quad (6)$$

Eq. (7) shows the relationship between the zenith angle θ_z (the angle between the zenith -the line normal to the ground- and the sun), the declination angle δ, the hour angle ω, and the latitude angle ϕ[41].

$$\cos(\theta_z) = \cos(\delta).\ \cos(\omega).\ \cos(\phi) + \sin(\delta).\ \sin(\phi) \quad (7)$$

After calculating the incidence angle using the optical model of the PTC, the solar power absorbed by the PTC ($\dot{Q}_{abs}$) is given by [42]:

$$\dot{Q}_{abs} = \eta_o.\ DNI.\ \cos(\theta).\ A_p.\ IAM \quad (8)$$

where, $\eta_o = 0.748$ is the optical efficiency of the collectors [38]; DNI is the direct normal irradiance; A_p is the area of the aperture; and IAM is the incident angle modifier taken from table based values provided by the PTC manufacturer [38]. Note that, in Eq. (8), the effects of the incidence angle and the IAM are considered separately.

The heat losses in the PTC ($\dot{Q}_{loss}$) are predicted using the following correlation [42]:

$$\dot{Q}_{loss} = a_0 + a_1.\ (T_{htf} - T_{amb}) + a_2.\ (T_{htf} - T_{amb})^2 \quad (9)$$

where, $a_0 = a_2 = 0$ and $a_1 = 0.64$ are the heat loss coefficients taken from the PTC datasheet [38], and T_{amb} is the temperature of the outdoor ambient air. The temperature of the heat transfer fluid (HTF) is assumed to be increasing linearly through the collectors, hence T_{htf} is the average HTF temperature in the collectors:

$$T_{htf} = \frac{T_{htf,in} + T_{htf,out}}{2} \quad (10)$$

where, $T_{htf,out}$ and $T_{htf,in}$ are, respectively, the outlet and inlet temperatures of the HTF in the PTC solar array.

Finally, the thermal power generated by the PTC in the PTC solar array is

$$\dot{Q}_{SOL} = \dot{Q}_{abs} - \dot{Q}_{loss} \quad (11)$$

The HTF temperature is increased by $\Delta T = 40$ °C through the PTC solar array by controlling the mass flow rate of the HTF ($\dot{m}_{htf}$) so that $T_{htf,in} = 140$ °C and $T_{htf,out} = 180$ °C.

The power consumption of the recirculation pump is calculated by:

$$P_e = \frac{P_{htf}}{\eta_{recir}} \quad (12)$$

where, η_{recir} is the recirculation pump efficiency, and P_{htf} is the pump power required for recirculating the HTF:

$$P_{htf} = \dot{m}_{htf} \frac{\Delta p}{\rho_{htf}} \quad (13)$$

where, $\dot{m}_{htf}$ is the HTF mass flow rate in the PTC solar array and ρ_{htf} is the HTF density. The correlation for estimating the pressure drop in the PTC solar array (Δp) is taken from the PTC data sheet [38].

$$\Delta p = 1.24 \times 10^{-4} \times \dot{m}_{htf}^2 + 1.27 \times 10^{-3} \times \dot{m}_{htf} \quad (14)$$

Experimental data from the manufacturer Soltigua [43] was used to validate the PTMx-24 collector model in this work. In Fig. 3, the control-oriented model of the PTC was used to estimate the generated thermal power, at the nominal operating point, with respect to the number of collectors. The results show that the PTC model is in good agreement with the manufacturer data.

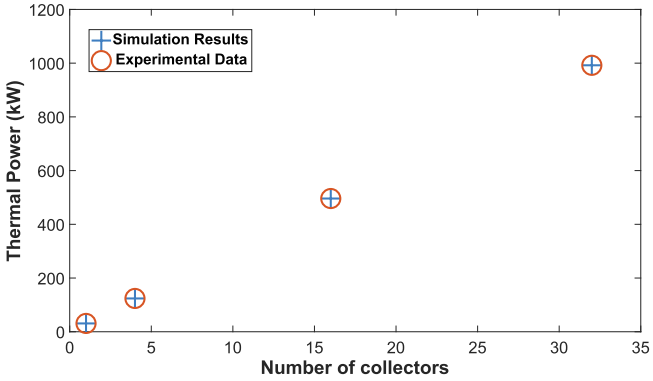

Fig. 3. PTC model validation with manufacturer thermal power data [43] for different number of collectors.

3.2. PV panel model

In this paper, the well-known single-diode equivalent circuit of PV cells is used to develop a five-parameter model of the PV panel [44]. The equivalent circuit of PV cells includes a series and a shunt resistance and a current source in parallel with a diode. Details of the PV panel mathematical model can be found in [29,35]. The PV panel modeled in this work includes the "KD210GX-LP" PV panel model manufactured by Kyocera Solar Solutions [45]. The PV panel model has been experimentally validated in our previous work in reference [35]. Fig. 4 shows a very good agreement between the estimated and the measured output power of the PV panel.

3.3. TES and BES models

In this study, the TES system is used as a buffer to mitigate intermittent thermal power supply from the PTC solar array and guarantee

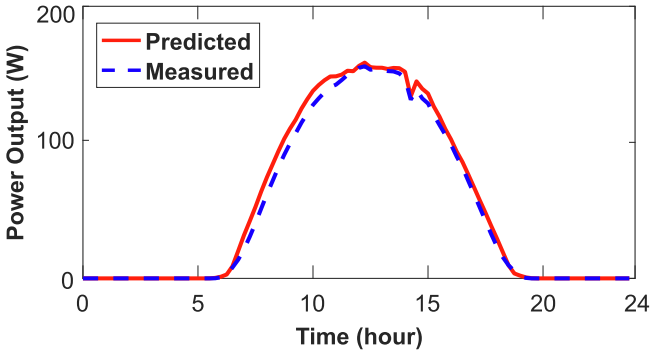

Fig. 4. PV panel validation result for Kyocera 210 KD210GX-LP Solar Panel.

reliable and efficient power generation from the ORC despite the stochastic nature of solar irradiation.

As shown in Fig. 1(a), the TES system is composed of a two-tank direct system. Each tank is modeled as a fully-mixed tank with a cylindrical shape that can contain the entire quantity of the HTF. During charging, the high-temperature HTF produced by the PTC solar array accrues in the hot tank, while the low-temperature HTF from the cold tank is fed back to the PTC solar array. During discharging, the high-temperature HTF accumulated in the hot tank is supplied to the ORC that converts the thermal energy contained in the HTF into electrical energy and cogenerated heat then rejects the low-temperature HTF to the cold tank. The tanks are assumed to be well insulated. Since overnight storage is not provided, the heat losses from the tanks are neglected. Indeed, the PTC solar array production is stored so that it can be used to run the ORC at its maximum efficiency during the occupancy period when thermal and electrical energies are needed.

To estimate the rate of change in the SOC of the TES, the following equation is used:

$$\dot{SOC}^{TES} = \frac{\dot{Q}_{SOL} - \dot{Q}_{TES}}{C_{TES}} \tag{15}$$

where, $\dot{Q}_{SOL}$ is the thermal power production of the PTC solar array, $\dot{Q}_{TES}$ is the thermal power output from the TES to the ORC, and C_{TES} is the TES thermal capacity.

In the PV based system, the BES system is a set of lithium-ion air-cooled battery packs, model "RESU" manufactured by LG Chem with a nominal capacity of 6.5 kWh (Fig. 1(b)). The battery packs are modeled based on the performance map provided by the manufacturer [46]. Using the battery performance map, the temperature and the maximum charge and discharge powers at a given SOC are derived [47].

The rate of change in the SOC of the BES is estimated using the following equation [47]:

$$\dot{SOC}^{BES} = \frac{P_{PV} - P_{S2B}}{V_B C_{BES}} \tag{16}$$

where, P_{PV} is the electrical power production of the PV solar array and P_{S2B} is the power dispatched from the BES to the building, V_B is the voltage across the battery, and C_{BES} is the battery's capacity.

For optimal usage of the storage capacity and flexible operation of the MPC, the TES and BES should be properly sized. In this study, an iterative approach was used to investigate the effect of sizing on the system performance. Hence, the TES and BES capacities were chosen to correspond to 98% of the maximum possible cost saving. More details about energy storage sizing are provided in Section 5.6.

3.4. ORC model

In this paper, a low-temperature ORC engine with a 10 kW nominal power manufactured by ENOGIA, model ENO-10LT [48] is considered. R245fa is used as the working fluid (WF) in the ORC cycle. As shown in Fig. 5, the HTF dispatched by the TES transfers its thermal energy to the WF through the evaporator that changes the WF state to vapor. The resulting high-temperature high-pressure vapor goes through the turbine (State 1) that converts its energy into mechanical work which will be converted into electricity by the power generator. This reduces the WF pressure and temperature while remaining at a vapor state (State 2). The WF is then condensed after transferring its thermal energy to the coolant in the condenser heat exchanger. The extracted heat will be used to preheat the air supplied to the thermal zones. The resulting low-temperature low-pressure liquid (State 3) is recirculated through a pump increasing its pressure (State 4) transferring it back to the evaporator, and the cycle is repeated.

The First Law of Thermodynamics (FLT) is applied to the WF closed system to derive the ORC governing equations:

$$\dot{Q}_{TES} = \dot{m}_{tes}.\, c_{p,htf}.\, (T_{ev,in} - T_{ev,out}) \tag{17a}$$

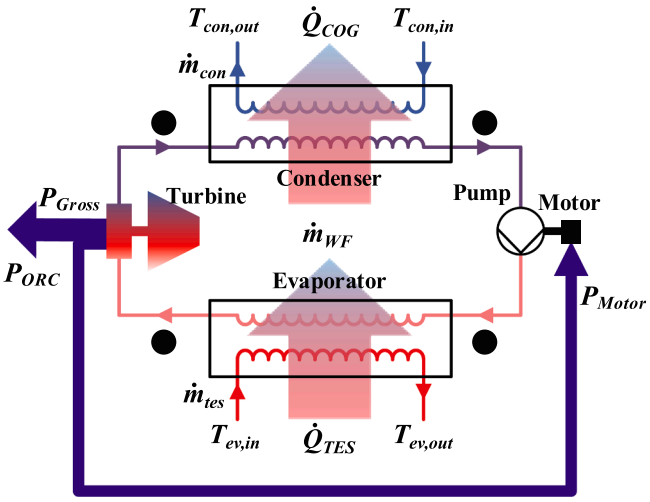

Fig. 5. Schematic of the ORC in this study.

$$P_{ORC} = P_{gross} - P_{pump} \tag{17b}$$

$$P_{gross} = \eta_{gen}.\, \dot{m}_{wf}.\, (h_1 - h_2) \tag{17c}$$

$$P_{pump} = \frac{\dot{m}_{wf}.\, (h_4 - h_3)}{\eta_{pump}} \tag{17d}$$

$$\dot{Q}_{COG} = \dot{m}_{wf}.\, (h_2 - h_3) \tag{17e}$$

where, $\dot{Q}_{TES}$ is the thermal power dispatched to the ORC from the HTF; P_{ORC} and P_{gross} are the net and gross electrical power produced by the ORC turbine generator, respectively; P_{pump} is the power consumption of the recirculating pump; $\dot{Q}_{COG}$ is the thermal power cogenerated by the ORC; h_1, h_2, h_3, and h_4 are the WF enthalpies at the turbine inlet and outlet, and the pump inlet and outlet, respectively; η_{gen} and η_{pump} are, respectively, the efficiency of the ORC turbine generator and the efficiency of the recirculating pump; $\dot{m}_{tes}$ is the mass flow rate of the HTF dispatched from the TES and $\dot{m}_{wf}$ is the mass flow rate of the WF; $T_{ev,in}$ and $T_{ev,out}$ are the ORC evaporator's inlet and outlet temperatures, respectively.

It can be shown that

$$P_{ORC} = f(\dot{m}_{wf}, \dot{m}_{tes}, c_{p,htf}, T_{ev,in}, T_{ev,out}, h_3, r_p, \eta_{gen}, \eta_{pump}) \tag{18a}$$

$$\dot{Q}_{COG} = g(\dot{m}_{wf}, \dot{m}_{tes}, c_{p,htf}, T_{ev,in}, T_{ev,out}, h_3, r_p, \eta_{gen}, \eta_{pump}) \tag{18b}$$

where, r_p is the ORC turbine pressure ratio (i.e., $r_p = \frac{P_1}{P_2}$).

In Eq. (18), $\dot{m}_{wf}$, $T_{ev,in}$, and $T_{ev,out}$ are constant design parameters. $c_{p,htf}$, η_{gen}, and η_{pump} are constant for the given working conditions. h_3 is constant since it is a function of the condensation pressure (P_3) and temperature (T_3) which are maintained constant by varying the mass flow rate of the coolant. The nominal value of 3 is chosen for the pressure ratio (r_p), which can be adjusted depending on the desired power, to maximize the efficiency of the ORC (η_{ORC}) at the nominal conditions. Considering all the assumptions above, it can be shown that P_{ORC} and $\dot{Q}_{COG}$ depend on $\dot{m}_{tes}$ only. Fig. 6 shows the variation of P_{ORC} and $\dot{Q}_{COG}$ as function of $\dot{m}_{tes}$.

Measurement data [36] from the manufacturer was used to validate the control-oriented model of the ORC at its nominal operation point. The results are shown in Table 2. The errors between measurements and model outputs are found to be less than 10%.

3.5. Building thermal model and HVAC power consumption

The thermal model of the building testbed studied in this paper is derived by applying the well-known RC modeling technique that uses resistive, capacitive, and current elements to model storage and heat

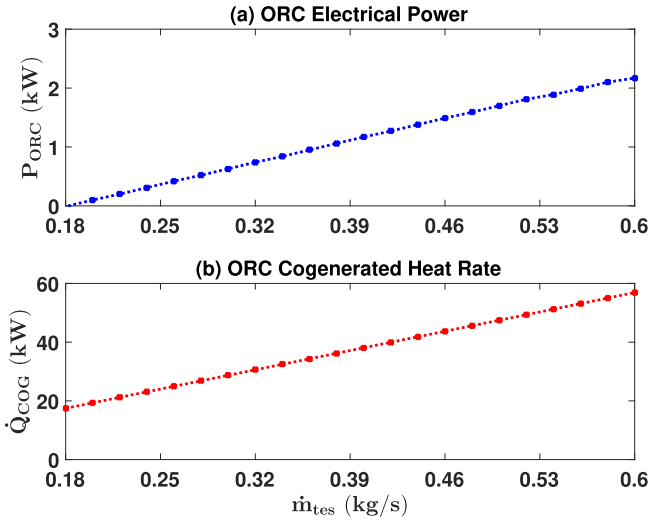

Fig. 6. Variation of the ORC output w.r.t. the input mass flow rate of the HTF ($\dot{m}_{tes}$): (a) electric power generation (P_{ORC}), and (b) thermal power generation ($\dot{Q}_{COG}$).

Table 2
ORC model validation against the manufacturer data [36] for the system nominal operating point. The inputs to the simulation model are $T_{ev,in}$, $T_{ev,out}$, P_1, T_1, P_3, T_3, and $\dot{m}_{tes}$ using the data provided by the manufacturer.

Variable	Unit	Measured	Simulated	Error (%)
$\dot{m}_{tes}$	kg/s	0.6	0.6	0.0
$\dot{Q}_{TES}$	kW	60	60.2	0.3
T_2	°C	73.8	71.9	2.6
T_4	°C	37	36.4	1.6
P_{gen}	kW	4	4	0.0
P_{pump}	kW	0.9	0.9	0.0
$\dot{Q}_{COG}$	kW	55	56.1	2.0

transfer with outdoor and neighboring thermal zones. The building testbed model is detailed and experimentally validated in our previous works in references [34,49,50]. The experimental validation of the building thermal model is presented in Fig. 7.

To calculate the energy consumption of the building HVAC system, the energy index ($I_{e,t}$) is determined by:

$$I_{e,t} = \sum_{t=0}^{24} \sum_{i=1}^{N_z} (P_{i,t}^F + P_{i,t}^H).\ \Delta t \tag{19}$$

where, N_z is the number of thermal zones in the building considered for this study. The main focus of this study is the heating mode, hence the HVAC electrical consumption is the total of the electrical power consumed by the HP ($P_{i,t}^H$) and by the ventilation fans ($P_{i,t}^F$). It is noteworthy that the MicroCSP can be used for cooling as well if an absorption chiller is integrated into the system [51]. However, in this study, we only focus on heating application.

The HP and ventilation fans electrical consumption are calculated by:

$$P_{i,t}^H = \frac{\dot{m}_{i,t}^{su}.\ c_{p,air}.\ (\mathscr{T}_{i,t}^{su} - T_{i,t}^{HP})}{COP} \tag{20a}$$

$$P_{i,t}^F = \gamma_F.\ (\dot{m}_{i,t}^{su})^3 \tag{20b}$$

where, $\dot{m}_i^{su}$ and $\mathscr{T}^{su}$ are the mass flow rate and the temperature of the supply air, respectively; $T_{i,t}^{HP}$ is the HP inlet air temperature; COP is the coefficient of performance of the HP; γ_F is the fan power coefficient.

During the non-occupancy period, the exhaust air from the thermal zones recirculates through the heat exchanger coupled with the ORC condenser before going to the HP. During the occupancy period, the ventilation requirements defined by the ANSI/ASHRAE Standard 62.1-2007 for required indoor air quality are considered. A 5 persons per 100 m^2 default occupant density of an office space and an 8.5 l/s per person default combined outdoor air rate are considered to estimate the minimum required mass flow rate ($\dot{m}_i^v$) of fresh air that will be mixed with the exhaust air from the thermal zones in the ERV. This mixed air passes through the ORC condenser and is heated, using the cogeneration heat ($\dot{Q}_{COG}$), to supply hot air to the HP or to the thermal zones directly. The inlet temperature of each individual HP is calculated using Eq. (21) for both occupancy and non-occupancy periods.

$$T_{i,t}^{HP} = \begin{cases} \dfrac{\left(\dot{m}_{i,t}^{su} - \dot{m}_{i,t}^{v}\right) T_{i,t}^{z} + \dot{m}_{i,t}^{v} T_t^{ERV}}{\dot{m}_{i,t}^{su}} + \dfrac{\dot{Q}_{COG,t}}{N_z \dot{m}_{i,t}^{r} c_{p,air}} & \text{(a) occupancy period} \\ T_{i,t}^{z} + \dfrac{\dot{Q}_{COG,t}}{N_z \dot{m}_{i,t}^{r} c_{p,air}} & \text{(b) non-occupancy period} \end{cases} \tag{21}$$

where, T^z is the temperature of the thermal zone. The temperature of the ERV outlet (T^{ERV}) is calculated as follows:

$$T_t^{ERV} = T_{amb,t} + ERE.\ (T_{i,t}^z - T_{amb,t}) \tag{22}$$

where, *ERE* is the energy recovery effectiveness of the ERV system defined by the AHRI (Air-Conditioning, Heating and Refrigeration Institute) Standard 1060 and the ASHRAE Standard 84.

4. Building model predictive control (MPC)

This section details the MPC design and optimization problem formulations for energy and cost minimization.

4.1. Energy optimization

Fig. 8(a) shows the structure of the MPC framework designed to minimize the electrical energy consumption of the building HVAC system equipped with the MicroCSP. At each time step Δt, the optimization problem is solved over the prediction horizon N. Eq. (23) defines the objective function while Eq. (24) lists the constraints. The optimized variables are the supply air temperature ($\mathscr{T}^{su}$), the HTF mass flow rate from the TES ($\dot{m}_{tes}$), and the slack variables ($\bar{\epsilon}$, $\underline{\epsilon}$) used to guarantee the existence of a feasible solution. The inputs to the MPC optimizer are solar irradiation and weather forecasts. The comfort temperature bounds are set based on ANSI/ASHRAE Standard 55-2013.

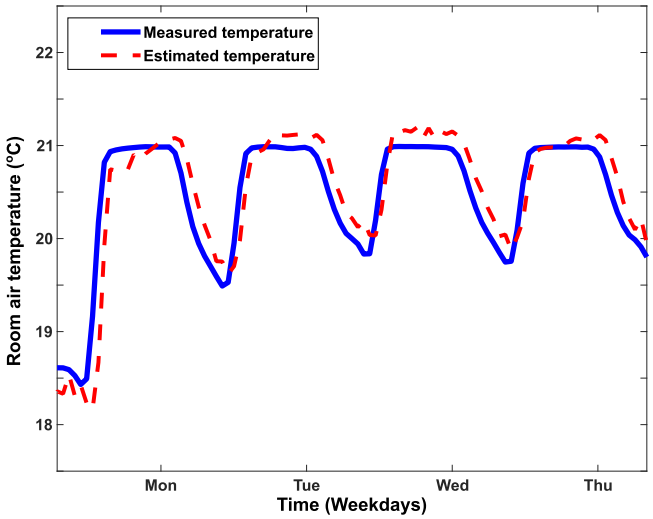

Fig. 7. Building thermal model validation result showing estimated and measured room temperature.

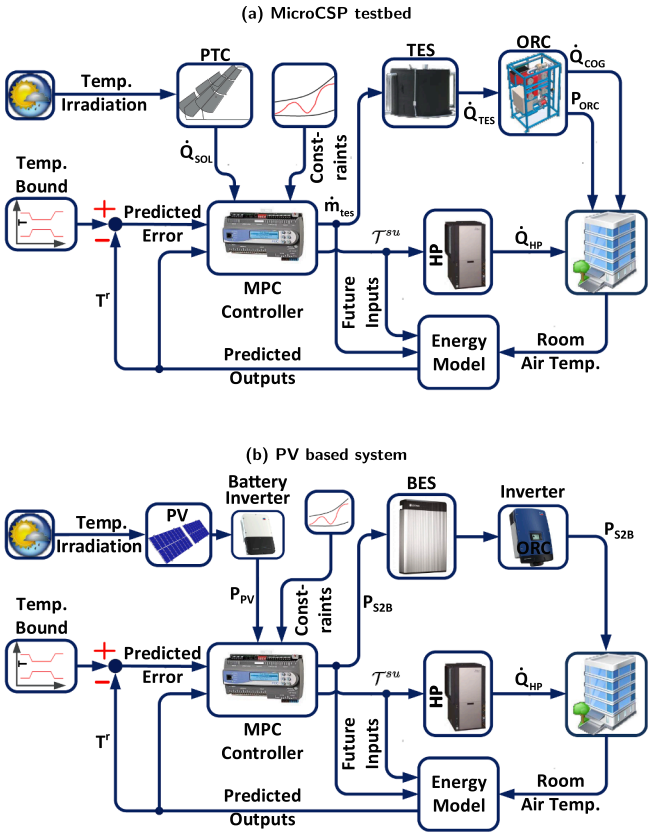

Fig. 8. Schematic diagram of the designed MPC framework for building HVAC energy and cost minimization.

$$\min_{\dot{m}_{tes},\mathscr{T}^{su},\bar{\epsilon},\underline{\epsilon}} \left\{ \overbrace{\left(I_{e,t} - \sum_{t=0}^{t_f} P_{ORC,t} \cdot \Delta t \right)}^{P_{Grid,t} \cdot \Delta t} + \rho \left(\left| \bar{\epsilon} \right|_1 + \left| \underline{\epsilon} \right|_1 \right) \right\} \tag{23}$$

Subject to the following constraints:

$$T_{t+k+1|t} = AT_{t+k|t} + B\mathscr{T}^{su}_{t+k|t} + Ed_{t+k|t} \tag{24a}$$

$$T^z_{t+k|t} = CT_{t+k|t} \tag{24b}$$

$$P_{ORC,t+k|t} = f(\dot{m}_{tes_{t+k|t}}) \tag{24c}$$

$$\dot{Q}_{COG,t+k|t} = g(\dot{m}_{tes_{t+k|t}}) \tag{24d}$$

$$SOC^{TES}_{t+k+1|t} = SOC^{TES}_{t+k|t} + \frac{\sum_{t+k|t}^{t+k+1|t} \left(\dot{Q}_{SOL_{t+k|t}} - \dot{Q}_{TES_{t+k|t}} \right) \cdot \Delta t}{C_{TES}} \tag{24e}$$

$$SOC^{TES}_1 = SOC^{TES}_{t_{max}} \tag{24f}$$

$$\underline{SOC}^{TES} \leqslant SOC^{TES}_{t+k+1|t} \leqslant \overline{SOC}^{TES} \tag{24g}$$

$$0 \leqslant \dot{m}_{tes_{t+k|t}} \leqslant \dot{m}_{max} \tag{24h}$$

$$T^{HP}_{t+k|t} \leqslant \mathscr{T}^{su}_{t+k|t} \leqslant \bar{\mathscr{T}}_{t+k|t} \tag{24i}$$

$$\underline{T}^r_{t+k|t} - \underline{\epsilon}_{t+k|t} \leqslant T^z_{t+k|t} \leqslant \overline{T}^r_{t+k|t} + \bar{\epsilon}_{t+k|t} \tag{24j}$$

$$\underline{\epsilon}_{t+k|t},\ \bar{\epsilon}_{t+k|t} \geqslant 0 \tag{24k}$$

The state-space Eqs. (24a) and (24b) capture the thermodynamics of the building; Eqs. (24c) and (24d) include the ORC model; the SOC of the TES is estimated in Eq. (24e); Eq. (24f) presents the charge sustaining constraints of the TES; Eq. (24g) defines the upper and lower bounds of the TES SOC set to 95% and 5%, respectively; Eq. (24h) is the maximum HTF mass flow rate ($\dot{m}_{max}$) dictated by the ORC manufacturer [48]; Eq. (24i) shows the constraints on the supply air temperature that represents the constraint on the control input; Eq. (24j) defines the comfort temperature bounds of the thermal zone temperature and includes the slack variables; finally, Eq. (24k) presents the slack variables constraints.

The structure of the designed MPC framework for optimal energy control of the building HVAC system equipped with the PV system is depicted in Fig. 8(b). For building HVAC energy consumption minimization, the objective function and the corresponding constraints are defined in Eq. (25) and Eq. (26), respectively.

$$\min_{P_{S2B},\mathscr{T}^{su},\bar{\epsilon},\underline{\epsilon}} \left\{ \overbrace{\left(I_{e,t} - \sum_{t=0}^{t_f} P_{S2B,t} \cdot \Delta t \right)}^{P_{Grid,t} \cdot \Delta t} + \rho \left(\left| \bar{\epsilon} \right|_1 + \left| \underline{\epsilon} \right|_1 \right) \right\} \tag{25}$$

The optimization problem is subject to the constraints listed bellow:

$$T_{t+k+1|t} = AT_{t+k|t} + B\mathscr{T}^{su}_{t+k|t} + Ed_{t+k|t} \tag{26a}$$

$$T^z_{t+k|t} = CT_{t+k|t} \tag{26b}$$

$$SOC^{BES}_{t+k+1|t} = SOC^{BES}_{t+k|t} + \frac{\sum_{t+k|t}^{t+k+1|t} \left(P_{PV_{t+k}} - P_{S2B_{t+k}} \right) \Delta t}{V_{B_{t+k}} C_{BES}} \tag{26c}$$

$$SOC^{BES}_1 = SOC^{BES}_{t_{max}} \tag{26d}$$

$$\underline{SOC}^{BES} \leqslant SOC^{BES}_{t+k+1|t} \leqslant \overline{SOC}^{BES} \tag{26e}$$

$$0 \leqslant P_{PV_{t+k|t}} \leqslant f_{chg}(SOC^{BES},\ T_{amb}) \tag{26f}$$

$$0 \leqslant P_{S2B_{t+k|t}} \leqslant f_{dschg}(SOC^{BES},\ T_{amb}) \tag{26g}$$

$$T^{HP}_{t+k|t} \leqslant \mathscr{T}^{su}_{t+k|t} \leqslant \bar{\mathscr{T}}_{t+k|t} \tag{26h}$$

$$\underline{T}^r_{t+k|t} - \underline{\epsilon}_{t+k|t} \leqslant T^z_{t+k|t} \leqslant \overline{T}^r_{t+k|t} + \bar{\epsilon}_{t+k|t} \tag{26i}$$

$$\underline{\epsilon}_{t+k|t},\ \bar{\epsilon}_{t+k|t} \geqslant 0 \tag{26j}$$

The building thermodynamics are captured by the state-space Eqs. (26a) and (26b); Eq. (26c) estimates the SOC of the BES; the BES charge sustaining constraints are presented in Eq. (26d); Eq. (26e) is used to reduce losses and aging of battery [52] by defining the upper and lower bounds of the BES SOC set to 70% and 30%, respectively, as suggested by the BES manufacturer; Eqs. (26f) and (26g) represent the charge and discharge rate limitations derived from the performance maps of the battery packs as functions of the SOC and the temperature of the battery; Eq. (26h) includes the constraint on the supply air temperature which is the control input; Eq. (26i) is used to keep the temperature of the thermal zone within the comfort temperature bounds while including the slack variables; Eq. (26j) shows the constraint on the slack variables.

4.2. Cost optimization

The objective function in Eq. (27) is used for energy cost minimization of the building HVAC system with MicroCSP. The building power consumption in the objective function is multiplied by locational marginal pricing (LMP) of electricity. The LMP data is provided by the Midcontinent Independent System Operator (MISO) at most 24 h in advance [53]. The optimization problem is solved for the following objective function subject to the same constraints listed in Eq. (24).

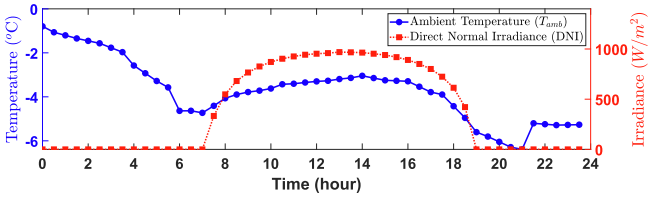

Fig. 9. Ambient air temperature (T_{amb}) and Direct Normal Irradiance (DNI) measurements from March 18, 2016, in Houghton, MI.

$$\min_{\dot{m}_{tes},\mathscr{T}^{su},\bar{\epsilon},\underline{\epsilon}} \left\{ \overbrace{\left(I_{e,t} - \sum_{t=0}^{t_f} P_{ORC,t}.\ \Delta t \right)}^{P_{Grid,t}.\Delta t} . \Omega^T + \rho \left(\left| \bar{\epsilon} \right|_1 + \left| \underline{\epsilon} \right|_1 \right) \right\} \tag{27}$$

where, Ω^T is the LMP.

For the PV based system the objective function considered for the optimization problem is

$$\min_{P_{S2B},\mathscr{T}^{su},\bar{\epsilon},\underline{\epsilon}} \left\{ \overbrace{\left(I_{e,t} - \sum_{t=0}^{t_f} P_{S2B,t}.\ \Delta t \right)}^{P_{Grid,t}.\Delta t} . \Omega^T + \rho \left(\left| \bar{\epsilon} \right|_1 + \left| \underline{\epsilon} \right|_1 \right) \right\} \tag{28}$$

Subject to the same constraints listed in Eq. (26).

5. Control results

MATLAB® software was used to implement the building, PTC, PV panels, BES, TES, and ORC models. YALMIP Toolbox [54] was used in MATLAB® for the optimization problem formulation and providing an interface with the solver. IPOPT [55] and Gurobi [56] were used as solvers, and the optimization problem was run in a computer with Intel® Core™i7-7500 CPU @ 2.90 GHz and 16.0 GB RAM.

The prediction horizon is $N = 48$, and the time step is $\Delta t = 30$ minutes. It is worth mentioning that the one-day ahead prediction constraint is dictated by the availability of the forecast data which is only available for the next 24 h. 72 thermal zones are considered for the building simulation. The simulations are performed using weather data from March 18, 2016, in Houghton, MI, USA, as shown in Fig. 9.

5.1. Optimal HVAC control

In this section, the MPC control results of the building HVAC without MicroCSP integration are presented. This section is included as the base case scenario for comparing its results with those of MicroCSP integration. The MPC framework formulation is similar to the objective function in the Eq. (23) but without the ORC power generation. The constraints are same as those in Eq. (24) excluding Eqs. (24c–h) representing the models and constraints appertaining to the ORC and the TES. The formulation of the optimization problem for optimal HVAC control is detailed in our previous work [49].

Fig. 10 depicts the temperature profiles of the supply air and a sample thermal zone, and the HVAC system power consumption. As seen in Fig. 10(a), the temperature of the thermal zone stays inside the comfort temperature bounds. Since the supply air temperature is the only control variable, the MPC minimizes the building HVAC energy consumption by keeping the thermal zone temperature at the lower comfort bound. HP receives power from the grid to increase the supply air temperature. Since HP are the only heat sources and only HVAC consumption is considered, the power supplied by the grid has a similar profile to the supply air temperature as shown in Fig. 10(b).

The temperature profiles of the supply air and a sample thermal zone, and the power consumed by the HP with respect to LMP are shown in Fig. 11. Fig. 11(a) shows that the MPC is increasing the thermal zone temperature without violating the comfort temperature bounds at periods where the LMP is low by supplying the maximum amount of heat from the HP, hence minimizing the cost of the HVAC system. Fig. 11(b) depicts the grid power supplied to the HP with respect to the LMP. In this case, the daily energy cost is 17$ compared to 37.8$ in the case of energy optimization.

5.2. Building predictive control with MicroCSP

Fig. 12(a) shows the temperature profiles of the supply air and a sample thermal zone within the comfort temperature bounds. From midnight to 6 AM, when the building is not occupied, the thermal zone temperature is allowed to fall down without violating the comfort bounds. Then, during the building occupancy, the HP supplies the minimum amount of heat to ensure that the thermal zone temperature stays at the lower comfort bound. Fig. 12(b) shows the heat produced in the PTC solar array, and the heat dispatched from the TES to the ORC. At the beginning and the end of the building occupancy, there is not enough heat production from the PTC solar array, hence the MPC uses the HP to supply the required heat to the thermal zone. When the TES is filled with enough quantity of heated HTF from the PTC solar array, the MPC runs the ORC to provide cogeneration heat to the building (Fig. 12(c)). Fig. 12(d) shows the power supplied from the power grid and from the ORC to the building. The MPC controls the PTC solar array production through the TES, regulating the input heat of the ORC to operate at its maximum efficiency and provide cogeneration heat to keep the thermal zone at the lower comfort bound. This causes the SOC of the TES to vary, as shown in Fig. 12(e).

The MPC results for minimizing HVAC operational cost are shown in Fig. 13. Fig. 13(a) shows the temperature profiles of the supply air and a sample thermal zone within the comfort temperature bounds. It can be seen that from midnight to 4 AM when the building is not occupied, the HP are turned off as the thermal zone temperature is within the comfort temperature bounds. Then, at 4:30 AM when the LMP is low, the MPC is preheating the room to guarantee that the thermal zone temperature does not fall below the lower comfort bound. During the building occupancy, the MPC tries to maintain the thermal zone temperature close to the lower comfort bound to avoid spending unnecessary energy. Fig. 13(b) shows the thermal power generated by the PTC solar array and the TES thermal power supplied to the ORC. As shown in Fig. 13(c), the MPC turns on the HP around 4:30 PM to preheat the thermal zone when the LMP is low. Then, when the PTC solar array starts producing enough heat, the HP supplies heat to the thermal zone using cogeneration heat from the ORC and switch to the HP only when the LMP is low again (3 PM). Fig. 13(d) depicts the grid power consumed by the HP as a response to the LMP variations. The TES stores the extra heat generated by the PTC solar array that is not used by the ORC so that it can be utilized later, at the end of the day when the solar irradiation is not enough to produce heat in the PTC solar array. The variation of the SOC of the TES is shown in Fig. 13e) and confirms that all the solar energy is used; thus, the initial and final SOCs are the same.

5.3. Rule-based control with MicroCSP

The most commonly used controllers for building HVAC systems are the rule-based controllers (RBC) due to their simplicity and easy implementation. To guarantee thermal comfort, the RBC checks the thermal zone temperature at each time step. When the thermal zone temperature is outside the comfort temperature bounds, the RBC switches on the heating or cooling elements for the time step period Δt until it is again within the comfort temperature bounds. Here, the RBC results are explained since they provide a baseline to compare with MPC results for the MicroCSP system to assess the impact of the predictive model-based control strategy on saving HVAC energy or cost.

Fig. 14 depicts the RBC results for MicroCSP integration into the

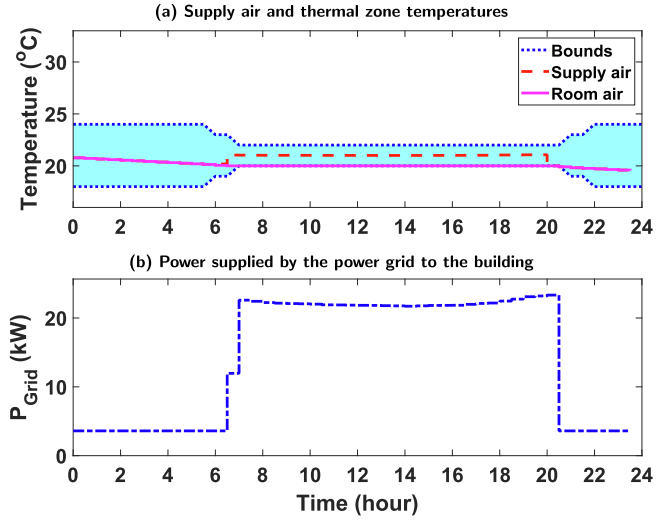

Fig. 10. MPC results with *minimal HVAC energy consumption* for a sample thermal zone in the building *without MicroCSP integration*.

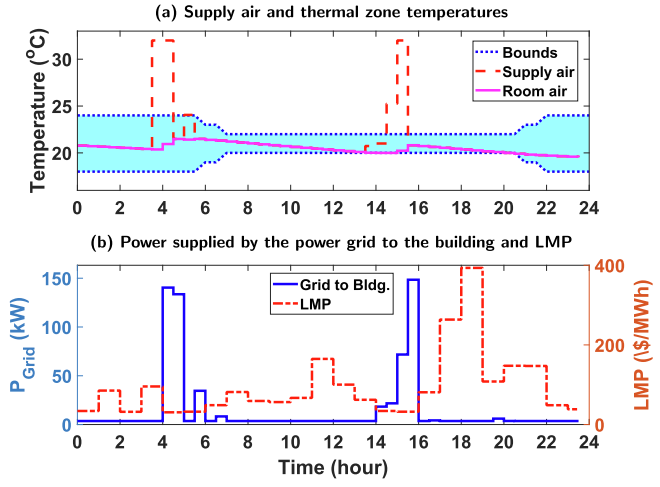

Fig. 11. MPC results with *minimal HVAC energy cost* for a sample thermal zone in the building *without MicroCSP integration*.

building. As it can be seen in Fig. 14(a), when the thermal zone temperature violates the comfort temperature bounds at 7 AM and 9 PM, the RBC turns on the HP to increase the thermal zone temperature and bring it within the comfort temperature bounds. Starting from 8 AM, the MicroCSP uses the maximum amount of thermal energy cumulated in the TES from the PTC solar array (Fig. 14(b)). From Fig. 14(c), it can be seen that the HP operates only when the comfort temperature bounds are violated while the ORC heat production supplies heat to the thermal zone as long as it is available, keeping its temperature within the comfort temperature bounds. Fig. 14(d) depicts the power supplied to the HP by the grid and the LMP. Since the solar energy production is directly injected into the ORC without any dispatch, the SOC does not vary much, as it is shown in Fig. 14(e).

The building occupancy coincides with the sunlight period; hence, the thermal zones are heated using cogeneration heat from the MicroCSP keeping their temperature inside the comfort bounds. However, when the MicroCSP is off, the thermal zone temperature falls down until it violates the comfort temperature bounds only then the RBC turns on the HP to bring back the thermal zone temperature inside the comfort temperature bounds which leads to high energy consumption. Since this violation occurs in periods when LMP is high (Fig. 14) it leads to higher costs as well. The predictive capability of the MPC anticipate these temperature violations and turn on the HP to

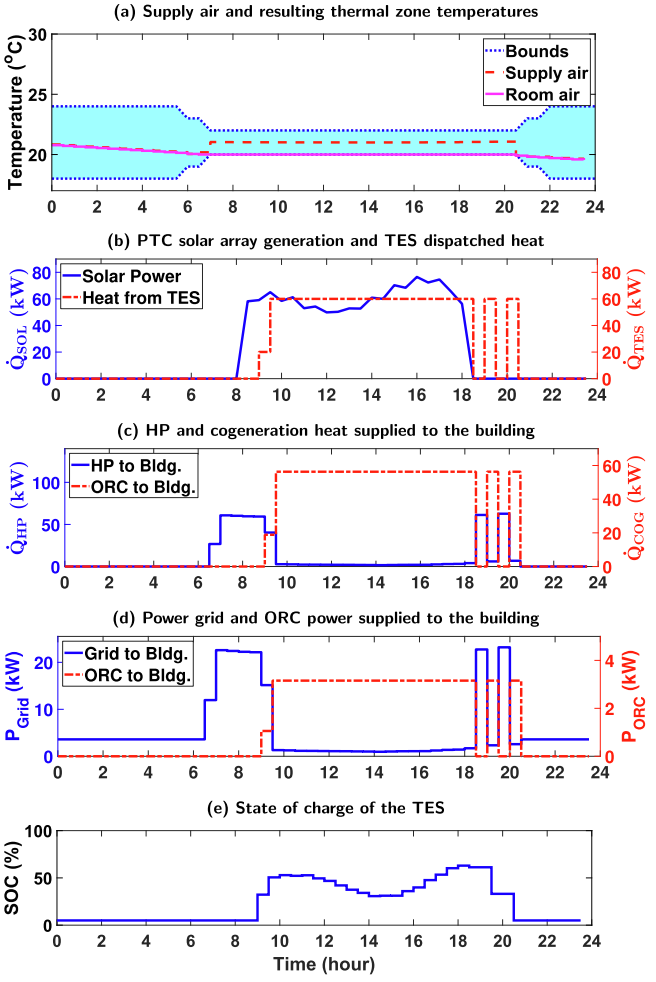

Fig. 12. *MPC results for energy minimization with MicroCSP* integrated into the building HVAC system.

preheat the thermal zone when the MicroCSP is off (Fig. 12) or when the LMP is low (Fig. 13).

Table 3 presents the energy consumption and energy cost saving by integrating the MicroCSP into the building HVAC system using RBC compared to MPC. The savings are calculated by reference to MPC based control of the HVAC system without MicroCSP integration.

The integration of MicroCSP into the building HVAC system reduces the energy consumption by about 39% while the cost of electricity increases by about 27% with RBC compared to the building HVAC system without MicroCSP integration using MPC. However, by designing an MPC framework for the control of the MicroCSP integrated into the building HVAC system, the energy and cost savings increase to 61% and 62%, respectively. This shows the importance of the MPC framework to exploit the full potential of the MicroCSP thermal and electrical production when integrated into the building HVAC system.

5.4. Building predictive control with PV

Fig. 15(a) shows the temperature profiles of the supply air and a sample thermal zone within the comfort temperature bounds. When the building is not occupied from midnight to 6 AM, the controller allows the thermal zone temperature to fall down without violating the comfort temperature bounds. Then, during the building occupancy, the HP supplies the minimum amount of heat to ensure that the thermal zone temperature stays at the lower comfort bound. Note that the temperature profiles are similar to those of the MicroCSP system. This can be explained by the fact that both TES and BES are sized to store the excess

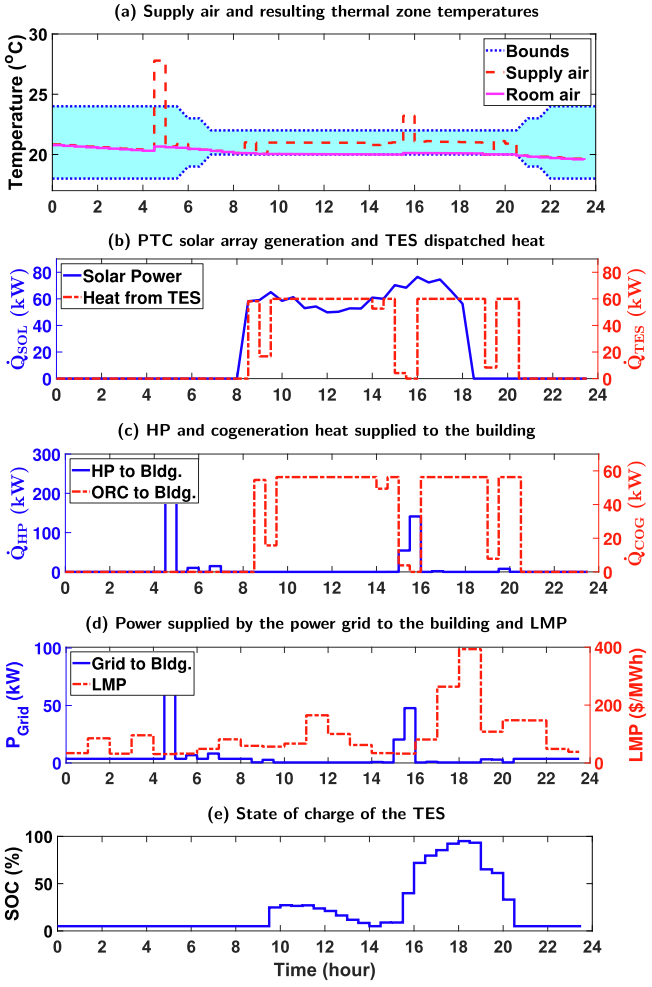

Fig. 13. *MPC results for cost minimization with MicroCSP* integrated into the building HVAC system.

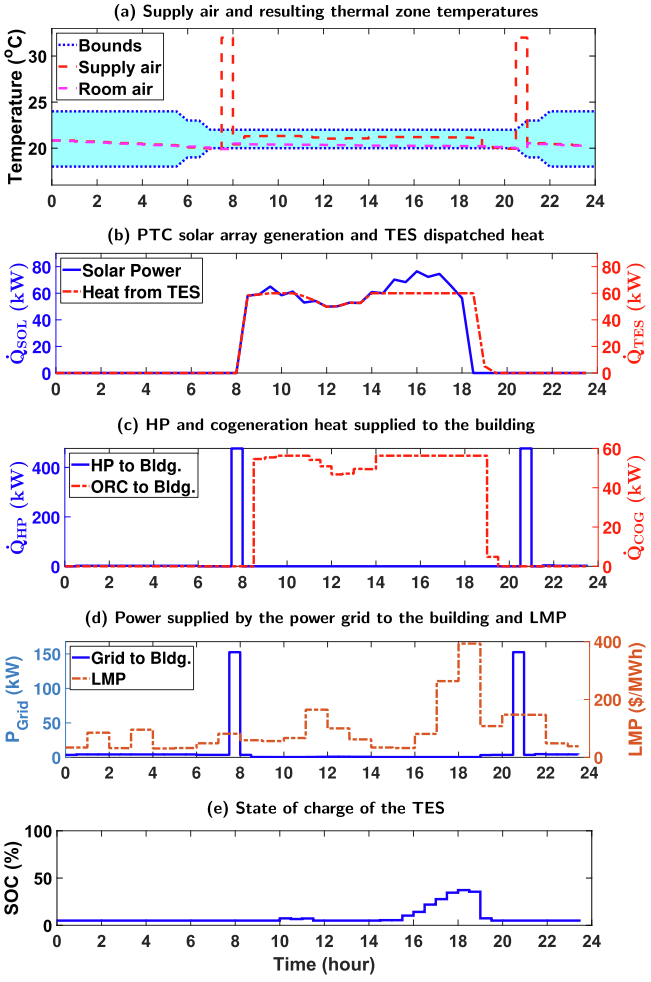

Fig. 14. *RBC results with MicroCSP* integrated into the building HVAC system.

heat/power that remains after supplying the minimum heat required by the building. This avoids unnecessary increase in the thermal zone temperature. Fig. 15(b) shows the power produced by the PV solar array. Since all the PV solar array production is meant to be consumed by the HP and there are no price incentives, the controller is feeding all the power available from the PV solar array to the HP through the BES (Fig. 15(c)). Hence, as it can be seen from Fig. 15(d), the grid supplies power to the building only to compensate the PV solar array production. Fig. 15(e) shows the SOC of the BES, confirming all solar generated electrical energy is consumed by the end of the day (i.e., $SOC_1^{BES} = SOC_{t_{max}}^{BES}$).

The results of minimizing HVAC operational cost are shown in Fig. 16. Fig. 16(a) depicts the temperature profiles of the supply air and a sample thermal zone within the comfort temperature bounds. Notice that, before 4 AM, the MPC turns off the HP letting the temperature of thermal zone fall down inside the comfort temperature bounds since the building is not occupied. Then, the MPC preheats the thermal zone before the beginning of the occupancy period (i.e., 7 AM to 8 PM), by turning on the HP when the LMP is low. During the building occupancy, the MPC first let the thermal zone temperature fall within the comfort temperature bounds then supplies the minimum amount of heat to keep it at the lower comfort bound until the LMP becomes low (i.e., 2 PM to 4 PM). Next, it heats the thermal zone at low LMP such that the thermal zone temperature stays within the comfort temperature bounds until the end of the day. Fig. 16(b) shows the power produced by the PV solar array. Arbitrage can be observed in Fig. 16(c) due to price incentives since the MPC shifts the PV solar array production to the periods where the LMP is high. Hence, as shown in Fig. 16(d), the grid supplies power to the building only when the LMP is low. Fig. 16(e) shows the MPC uses the maximum allowed battery capacity (i.e., $SOC^{BES} = 70\%$) and ensures that the initial and final SOC remain the same.

Table 3
Electrical energy consumption and cost comparison for showing the importance of integrating MicroCSP also the significance of using MPC control.

System	Control Type	Energy Consumption [kWh/day]	Energy Saving* [%]	Electricity Cost [$/day]	Cost Saving* [%]
HVAC	MPC	341.2	–	16.9	–
HVAC + MicroCSP	RBC	208.7	38.8%	21.5	−27.2%
HVAC + MicroCSP	MPC	130.3	61.8%	6.4	62.1%

*Calculated by reference to MPC based control of the HVAC system without MicroCSP integration.

5.5. MicroCSP and PV comparison

Table 4 provides the energy consumption and energy cost saving by utilizing MicroCSP integrated into the building HVAC system compared to those in the PV integration. The savings are calculated by reference to MPC based control of the building HVAC system without MicroCSP integration.

The integration of MicroCSP into the building HVAC system provides 61.8% energy savings and 62.1% cost saving compared to the building HVAC system without MicroCSP integration, using MPC

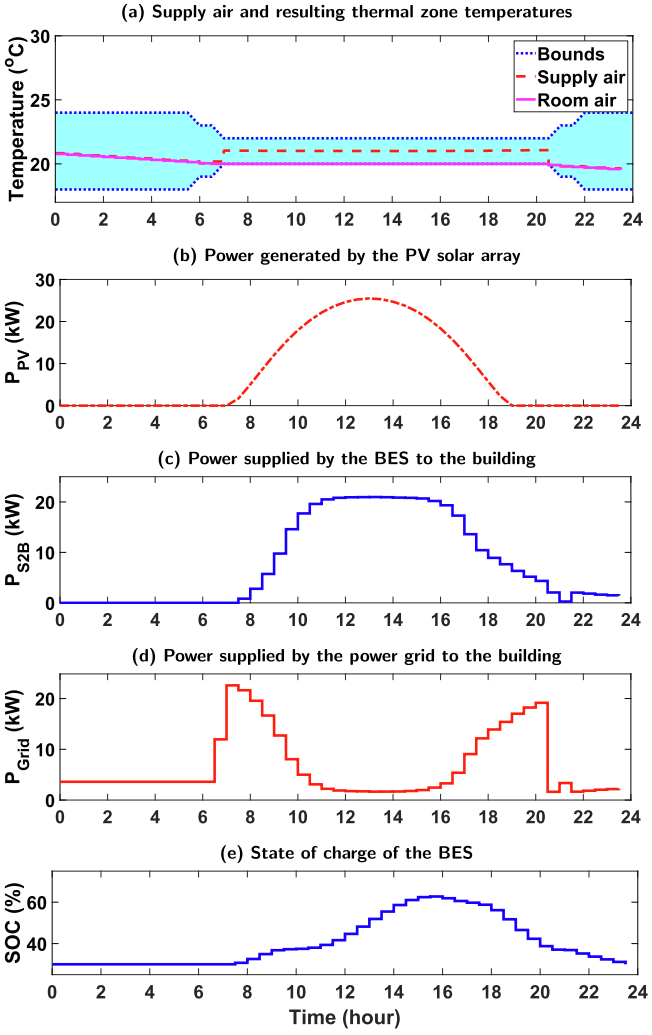

Fig. 15. *MPC results for energy minimization with PV* integrated into the building HVAC system.

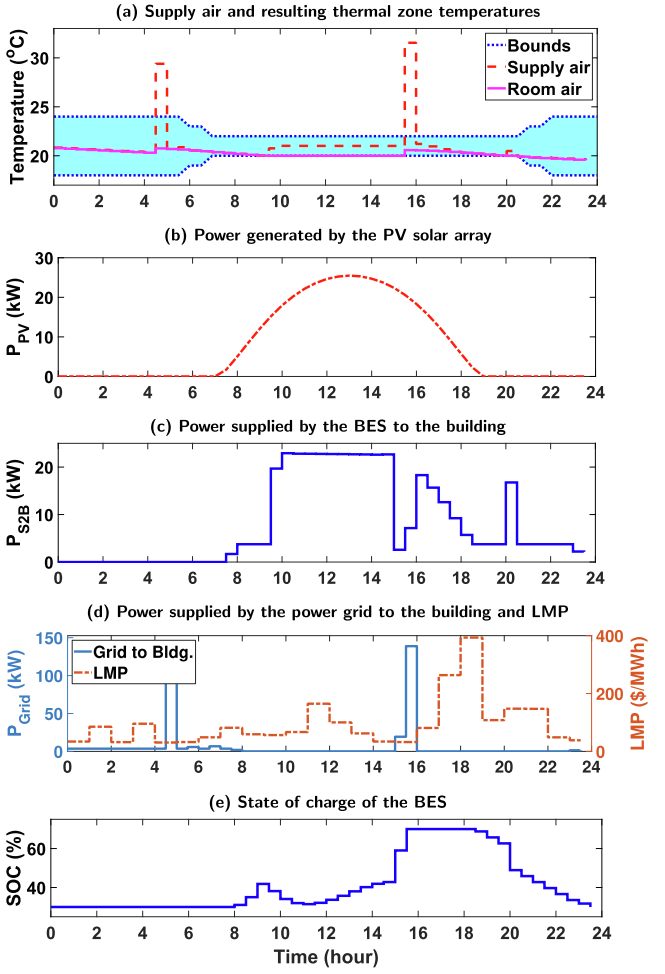

Fig. 16. *MPC results for cost minimization with PV* integrated into the building HVAC system.

framework. On the other hand, the PV integration into the building HVAC system ensured 53.8% and 65.8% energy saving and cost saving respectively, compared to the building HVAC system without MicroCSP integration, using MPC framework.

It can be seen that the PV integration provides around 3% more cost savings compared to the MicroCSP. However, when it comes to energy saving, the MicroCSP provides 8% more energy saving than that of the PV. This is due to the fact that the ORC is more efficient when it operates at its full capacity which makes it less flexible and responsive to the price variations in the case of cost minimization but more efficient when it comes to supplying steady energy production as in the case of energy minimization. The results of this study show that PV can be more practical for areas with variable electricity price due to the flexibility and high dispatchability of PV using BES, while MicroCSP is more suitable for areas with fixed electricity price since it offers both electricity and required HVAC heat; thus MicroCSP provides higher total required energy leading to higher energy saving.

5.6. Storage capacity effects

This section investigates into the effect of the size of TES and BES on the results of MicroCSP and PV integration into the building HVAC system in terms of energy consumption and cost.

Fig. 17(a) shows that TES size has more effect on the cost saving than the energy saving. The energy saving reaches its maximum value with a 38 kWh capacity TES and using a bigger TES does not lead to more energy saving. Indeed, for the actual penetration rate and without price incentives, the MicroCSP energy production does not need to be substantially dispatched as it can be consumed almost instantly by the building during the occupancy period. Still, minimum storage is required to guarantee that the ORC of the MicroCSP system is supplied with the nominal thermal power to operate at its maximum efficiency. On the other hand, increasing the TES capacity lowers the energy cost since it improves the system flexibility in terms of dispachability, so that MicroCSP production can supply the building at periods of high LMP as it is shown in Fig. 13. The energy cost saving reaches its maximum value starting from 114 kWh capacity.

In Fig. 17(b), a more remarkable observation should be pointed out in the case of energy consumption optimization with a PV system. In fact, the integration of storage, in this case, has led to an unexpected decrease in energy saving. Indeed, since the sunlight period coincides with the occupancy period where energy is required by the building and without price incentives, the PV solar array production can be injected directly to the system without the need to be stored and recovered later. This means that adding a BES system will not increase the energy saving. However, as we can see in Fig. 17(b), the integration of BES comes with the cost of adding an extra battery inverter that increases the conversion losses of the solar power which explains the higher energy saving when there is no BES system (the efficiency of the battery inverter is 96%, leading to almost 5% energy loss compared to the case when no BES is used.). For cost minimization, BES can help in performing arbitrage by dispatching the solar energy according to LMP as

Table 4
Electrical energy consumption and cost comparison among three different building HVAC systems.

System	Energy Consumption [kWh/day	Energy Saving* [%]	Electricity Cost [$/day]	Cost Saving* [%]
HVAC	341.2	–	16.9	–
HVAC + MicroCSP	130.3	61.8%	6.4	62.1%
HVAC + PV	157.7	53.8%	5.8	65.8%

*Calculated by reference to MPC based control of the HVAC system without solar energy integration.

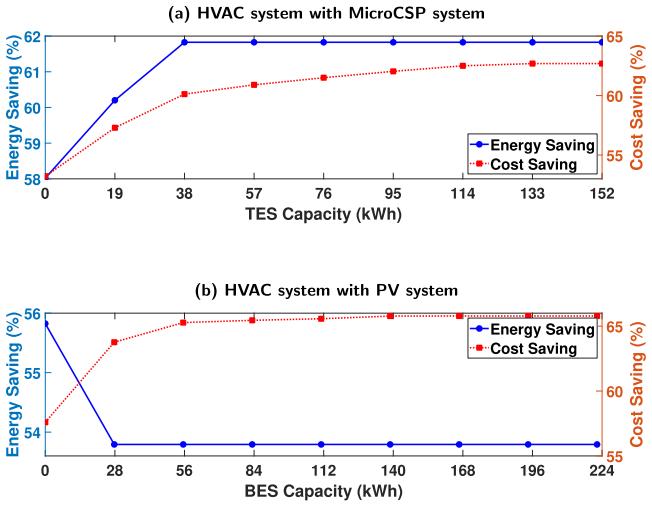

Fig. 17. Effects of storage capacity for the building HVAC daily energy consumption and daily electricity cost.

we can see in Fig. 16. The energy cost saving is significantly increased by increasing the BES capacity to 56 kWh. Above the capacity of 56 kWh, the slope of the energy cost saving becomes less significant and the cost saving reaches its maximum value starting from 168 kWh capacity. In this paper, optimum capacities of 95 kWh and 84 kWh for TES and BES were selected respectively since they provide over 98% of the maximum energy and cost savings.

5.7. Monte Carlo simulations

The MPC results can be subject to interpretation since they do not consider prediction uncertainty in LMP, solar irradiation, and variations in weather conditions. Hence, to demonstrate the performance of the designed MPC framework in the presence of variations and prediction uncertainties, a probabilistic Monte-Carlo analysis is carried out.

Reference [57] defines the accuracy of the temperature prediction as the percentage of forecasts within three degrees of Fahrenheit. According to reference [57] the accuracy of the temperature prediction is around 70% for the location of the testbed. Several parameters affect the forecast of solar irradiation which can be categorized into deterministic parameters (i.e., geographic coordinate, season, time of the day, etc.) and probabilistic parameters (i.e., weather, cloudiness, etc.). Authors in [58] have reported several techniques to forecast LMP with a mean absolute percent error (MAPE) ranging from 0.9% to 1.5%. Reference [59] presents a technique for forecasting solar irradiation with a MAPE of 9.1% for sunny days and 26.7% for cloudy days.

In this study, the Monte-Carlo analysis is performed by introducing additive uncertainty with a normal distribution to simulate random variations of the weather conditions, the solar irradiation, and the LMP using the results from [57–59]. The Monte-Carlo simulation results, depicted in Fig. 18–20, show the validity of the proposed methods with the presence of variations and prediction uncertainties.

Fig. 18(a) and (b) depict the probability distribution of the energy saving and cost saving, respectively, by applying MPC and utilizing MicroCSP compared to HVAC control without MicroCSP integration

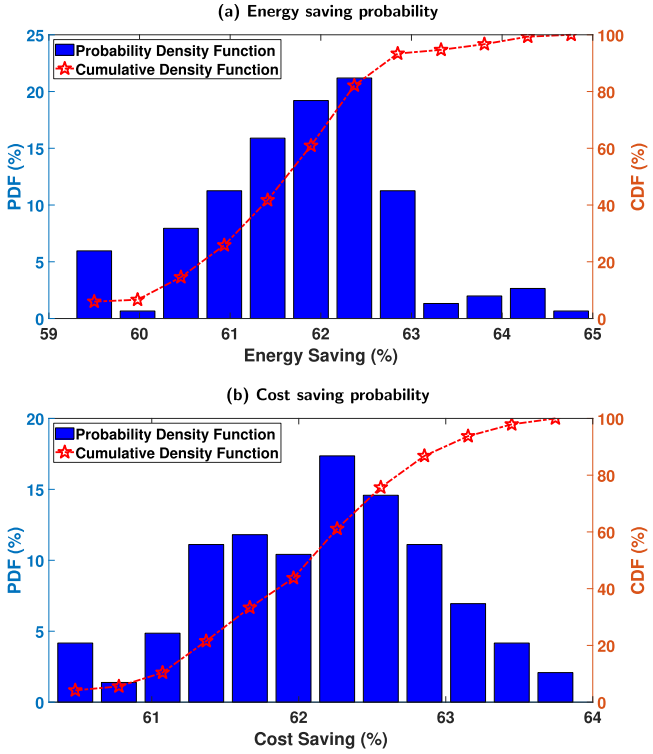

Fig. 18. *Monte-Carlo MicroCSP simulation results* showing the probability of the building HVAC energy and cost saving by applying MPC and utilizing MicroCSP, compared to HVAC control without MicroCSP using MPC framework.

using MPC framework. It is shown that the probability of at least 61% energy saving and 62% cost saving are 70% and 50%, respectively. Furthermore, Fig. 18 shows that in the worst case, the energy saving will drop to 59%, while the cost saving will drop to 60%.

Fig. 19(a) and (b) depict the probability distribution of the energy and cost savings of the building HVAC integrating MicroCSP by applying MPC, compared to using RBC. It can be seen that the probability of achieving at least 37% energy saving is around 60%, while the probability of at least 70% cost saving is 50%. Furthermore, it is shown that the energy saving will always be above 33% and the cost saving will always be above 68% in the worst case. This shows the significance of using MPC versus RBC for optimal operation of integrated HVAC and MicroCSP system.

The probability distribution of the energy saving and cost saving, by applying MPC and utilizing PV compared to HVAC control without MicroCSP integration using MPC framework, are shown in Fig. 20(a) and (b), respectively. The probability of at least 53% energy saving and 65% cost saving are over 70%, and at the worst case scenario, the energy saving will drop to 51%, while the cost saving will drop to 64%. By comparing Figs. 18 and 20, one can see the maximum energy saving by MicroCSP is 9% higher than that of the PV system, while the maximum cost saving by the PV system is 4% higher than that of the MicroCSP system.

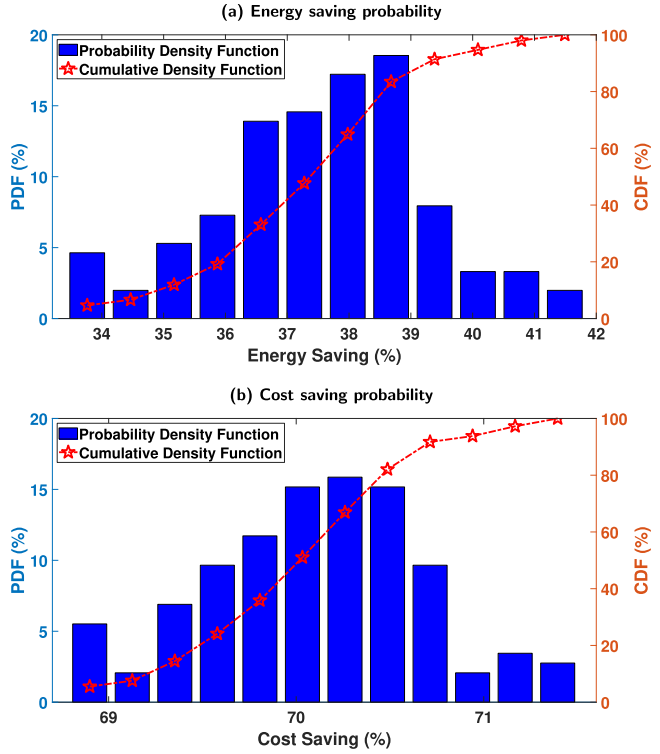

Fig. 19. *Monte-Carlo MPC simulation results* showing the probability of the building HVAC energy and cost saving by utilizing MicroCSP and applying MPC, *compared to using RBC.*.

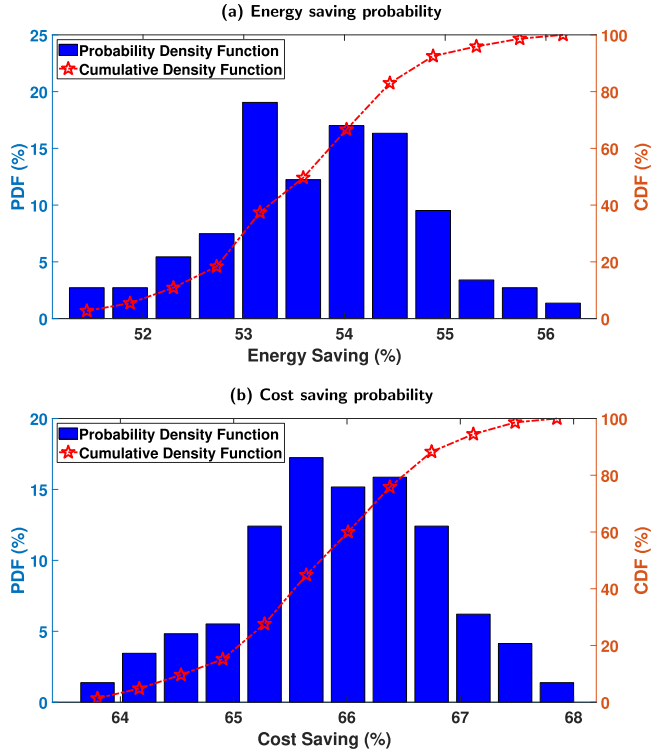

Fig. 20. *Monte-Carlo PV simulation results* showing the probability of the building HVAC energy and cost saving by applying MPC and utilizing PV, compared to HVAC control without PV using MPC framework.

6. Summary and conclusion

This paper presented a real-time model predictive control framework to minimize the energy consumption and operational cost of the building HVAC system with integrated MicroCSP. The proposed MicroCSP integration is compared, in terms of performance, to the conventional PV panel based system. In addition, a new control-oriented mathematical model of a MicroCSP system is derived. All MicroCSP and HVAC submodels were experimentally validated [34–36,43,49,50]. The key findings of this work are listed below:

Controller design effect: MPC vs. RBC

- The control results show that the design of an MPC framework for the MicroCSP integrated into the building HVAC system leads to a 37% energy saving compared to the conventional RBC. In other words, by understanding MicroCSP and HVAC dynamics, one can significantly reduce the energy consumption of the HVAC system. Furthermore, the designed MPC framework provides 70% reduction of the energy cost compared to the RBC. This shows that the MPC framework has more benefits when dealing with dynamic electricity prices due to its capability to optimize HVAC and MicroCSP energy flows by knowing the upcoming electricity price changes and acting accordingly.

Solar energy integration effect: MicroCSP vs. PV

- Integrating MicroCSP into the building HVAC system provides 62% energy saving versus 54% in the case of integrating PV, compared to the building HVAC system without solar energy integration, when MPC is utilized in all cases. However, when integrated into the building HVAC, the PV leads to more cost saving by providing 66% cost saving against 62% with MicroCSP integration, compared to the HVAC system without MicroCSP integration. Overall, MicroCSP provides more total energy (thermal + electrical) saving, while the PV combined with a BES system provides more flexible electrical energy for cost saving using arbitrage, compared to the MicroCSP system.

Energy storage sizing effect

- Proper energy storage sizing is essential to optimize the electrical cost and the energy consumption of the building HVAC system. Indeed, adding a TES system to the MicroCSP increases the energy saving by almost 4% and the cost saving by almost 10%. The integration of a BES system with the PV panels increases the cost saving by 8% while it decreases the energy saving by 2% due to the losses induced by the charging inverter. These numbers are only applicable to the conditions studied in this paper and can change when LMP profile or outdoor weather conditions change. Overall, the capacity of TES and BES need to be chosen carefully to avoid unnecessary oversizing since after reaching the optimal capacity, the cost and energy savings do not change any more even if the capacity is increased.

Prediction uncertainty and seasonal variation effects

- Monte Carlo analysis results show that, by utilizing MicroCSP and applying MPC, the HVAC energy saving ranges from 34% to 42% while the HVAC cost saving varies between 68% and 72% even in the presence of variations and prediction uncertainty, compared to using RBC. In addition, Monte Carlo simulations show that the energy saving and cost saving are within ± 5.5% and ± 4%, respectively for both MicroCSP and PV integration into the building HVAC system, compared to the HVAC system without a solar energy system.

A comprehensive economic study need to be carried out to address the financial aspects of integrating a MicroCSP into the building HVAC system. However, the concentration of this study is on the technical aspects. Our future work will include a more detailed study to perform an exergy analysis of the system and conduct a proper economical assessment of the MicroCSP system for building applications. Furthermore, the MPC controllers will be experimentally implemented and real-time demonstrations will be performed on the real testbed. Moreover, future works will also include building-to-grid integration with MicroCSP to design an optimization framework for demand-side response programs.

Declaration of Competing Interest

The authors declare that they have no known competing financial interests or personal relationships that could have appeared to influence the work reported in this paper.

Acknowledgments

This work was supported by the US National Science Foundation [Grant: #1541148]; the Richard and Elizabeth Henes Professorship of Mechanical Engineering at Michigan Technological University; and the Institute for Research on Solar and New Energies (IRESEN) in Morocco [Reference: InnoTherm-13-MicroCSP].

References

[1] Hansen J, Kharecha P, Sato M, Masson-Delmotte V, Ackerman F, Beerling DJ, Hearty PJ, Hoegh-Guldberg O, Hsu S-L, Parmesan C. Assessing dangerous climate change: required reduction of carbon emissions to protect young people, future generations and nature. PLoS One 2013;8(12):e81648.
[2] EPA. Inventory of U.S. Greenhouse Gas Emissions and Sinks: 1990–2016. URL:https://www.epa.gov/sites/production/files/2018-01/documents/2018_complete_report.pdf [accessed 24.05.2018].
[3] EIA. Electric power monthly with data for november 2017. URL:https://www.eia.gov/electricity/monthly/current-month/epm.pdf [accessed 24.05.2018].
[4] EIA. International energy outlook 2017.https://www.eia.gov/outlooks/aeo/pdf/0383(2017).pdf [accessed 18.01.2018].
[5] Steinfeld A, Palumbo R. Solar thermochemical process technology. Encyclopedia Phys Sci Technol 2001;15(1):237–56.
[6] Szabo S, Bódis K, Huld T, Moner-Girona M. Energy solutions in rural Africa: mapping electrification costs of distributed solar and diesel generation versus grid extension. Environ Res Lett 2011;6(3):034002.
[7] The SunShot Initiative — Department of Energy. URL:https://www.energy.gov/eere/solar/sunshot-initiative [accessed 12.07.2018].
[8] Department of Energy Announces $72 Million to Advance High-Temperature Concentrating Solar Power Systems. URL:https://www.energy.gov/eere/solar/generation-3-concentrating-solar-power-systems-gen3-csp [accessed 12.07.2018].
[9] Mueller A, Orosz M, Narasimhan AK, Kamal R, Hemond HF, Goswami Y. Evolution and feasibility of decentralized concentrating solar thermal power systems for modern energy access in rural areas. MRS Energy Sustain 2016;3:E4.
[10] Giovannelli A. State of the art on small-scale concentrated solar power plants. Energy Proc 2015;82:607–14.
[11] Oyewunmi OA, Kirmse CJ, Pantaleo AM, Markides CN. Performance of working-fluid mixtures in orc-chp systems for different heat-demand segments and heat-recovery temperature levels. Energy Convers Manage 2017;148:1508–24.
[12] Ramos A, Chatzopoulou MA, Freeman J, Markides CN. Optimisation of a high-efficiency solar-driven organic Rankine cycle for applications in the built environment. Appl Energy 2018;228:755–65.
[13] Mammoli A, Vorobieff P, Barsun H, Burnett R, Fisher D. Energetic, economic and environmental performance of a solar-thermal-assisted HVAC system. Energy Build 2010;42(9):1524–35.
[14] Ortiz M, Barsun H, He H, Vorobieff P, Mammoli A. Modeling of a solar-assisted HVAC system with thermal storage. Energy Build 2010;42(4):500–9.
[15] Mammoli A, Stadler M, DeForest N, Barsun H, Burnett R, Marnay C. Software-as-a-service optimised scheduling of a solar-assisted hvac system with thermal storage (Tech. rep). Berkeley, CA (U.S.): Lawrence Berkeley National Lab. (LBNL); 2012.
[16] Nguyen HT, Nguyen DT, Le LB. Energy management for households with solar assisted thermal load considering renewable energy and price uncertainty. IEEE Trans Smart Grid 2015;6(1):301–14.
[17] Ramos A, Chatzopoulou MA, Guarracino I, Freeman J, Markides CN. Hybrid photovoltaic-thermal solar systems for combined heating, cooling and power provision in the urban environment. Energy Convers Manage 2017;150:838–50.
[18] Gu Y, Zhang X, Myhren JA, Han M, Chen X, Yuan Y. Techno-economic analysis of a solar photovoltaic/thermal (PV/T) concentrator for building application in Sweden using Monte Carlo method. Energy Convers Manage 2018;165:8–24.
[19] Herrando M, Pantaleo AM, Wang K, Markides CN. Solar combined cooling, heating and power systems based on hybrid PVT, PV or solar-thermal collectors for building applications. Renew Energy 2019;143:637–47.
[20] Rodríguez LR, Lissén JMS, Ramos JS, Jara EÁR, Domínguez SÁ. Analysis of the economic feasibility and reduction of a building's energy consumption and emissions when integrating hybrid solar thermal/PV/micro-CHP systems. Appl Energy 2016;165:828–38.
[21] Cioccolanti L, Tascioni R, Bocci E, Villarini M. Parametric analysis of a solar organic rankine cycle trigeneration system for residential applications. Energy Convers Manage 2018;163:407–19.
[22] Alobaid F, Mertens N, Starkloff R, Lanz T, Heinze C, Epple B. Progress in dynamic simulation of thermal power plants. Prog Energy Combust Sci 2017;59:79–162.
[23] Powell KM, Rashid K, Ellingwood K, Tuttle J, Iverson BD. Hybrid concentrated solar thermal power systems: a review. Renew Sustain Energy Rev 2017;80:215–37.
[24] Kuravi S, Trahan J, Goswami DY, Rahman MM, Stefanakos EK. Thermal energy storage technologies and systems for concentrating solar power plants. Prog Energy Combust Sci 2013;39(4):285–319.
[25] Powell KM, Edgar TF. Modeling and control of a solar thermal power plant with thermal energy storage. Chem Eng Sci 2012;71:138–45.
[26] Camacho E, Rubio F, Berenguel M, Valenzuela L. A survey on control schemes for distributed solar collector fields. Part I: modeling and basic control approaches. Solar Energy 2007;81(10):1240–51.
[27] Camacho E, Rubio F, Berenguel M, Valenzuela L. A survey on control schemes for distributed solar collector fields. Part II: advanced control approaches. Solar Energy 2007;81(10):1252–72.
[28] Maasoumy M, Sangiovanni-Vincentelli A. Total and peak energy consumption minimization of building HVAC systems using model predictive control. IEEE Design Test Comput 2012;29(4):26–35.
[29] Razmara M, Bharati GR, Hanover D, Shahbakhti M, Paudyal S, Robinett RD. Enabling demand response programs via predictive control of building-to-grid systems integrated with PV panels and energy storage systems. Am Control Conf 2017;2017:56–61.
[30] Lešić V, Martinčević A, Vašak M. Modular energy cost optimization for buildings with integrated microgrid. Appl Energy 2017;197:14–28.
[31] Fiorentini M, Wall J, Ma Z, Braslavsky JH, Cooper P. Hybrid model predictive control of a residential HVAC system with on-site thermal energy generation and storage. Appl Energy 2017;187:465–79.
[32] Toub M, Reddy CR, Razmara M, Shahbakhti M, Robinett RD, Aniba G. Model predictive control for MicroCSP integration into a building hvac system. 2018 IEEE 14th International Conference on Control and Automation (ICCA). 2018. p. 890–5.
[33] Reddy CR, Toub M, Razmara M, Shahbakhti M, Robinett RD, Aniba G. Modeling and optimal control of micro-csp and a building hvac system to minimize electricity cost. ASME 2018 Dynamic Systems and Control Conference. American Society of Mechanical Engineers; 2018. pp. V002T28A004–V002T28A004.
[34] Maasoumy M, Razmara M, Shahbakhti M, Sangiovanni-Vincentelli A. Selecting building predictive control based on model uncertainty. Am Control Conf 2014.
[35] Razmara M, Bharati G, Hanover D, Shahbakhti M, Paudyal S, Robinett III R. Building-to-grid predictive power flow control for demand response and demand flexibility programs. Appl Energy 2017;203:128–41.
[36] Drouineau J. Technical communication with ENOGIA [accessed 28.08.2017].
[37] Lv Y, Si P, Rong X, Yan J, Feng Y, Zhu X. Determination of optimum tilt angle and orientation for solar collectors based on effective solar heat collection. Appl Energy 2018;219:11–9.
[38] Soltigua – Parabolic Troughs PTMx. URL:http://www.soltigua.com/ptmx-introduction/ [accessed 27.08.2017].
[39] Duffie JA, Beckman WA. Solar engineering of thermal processes. Ch. Solar Radiation.
[40] Spencer J. Fourier series representation of the position of the sun. Search 1971;2(5). 172–172.
[41] Cooper P. The absorption of radiation in solar stills. Solar Energy 1969;12(3):333–46.
[42] Burkholder F, Kutscher C. Heat loss testing of Schott's 2008 PTR70 parabolic trough receiver [Tech. rep.]. Golden, CO (United States): National Renewable Energy Lab. (NREL); 2009.
[43] Agenzia Nazionale per le Nuove tecnologie, l'Energia e lo Sviluppo economico sostenibile (ENEA). Performance test report summary according to EN 12975-2:2006, technical communication with SOLTIGUA [accessed 22.03.2017].
[44] Tian H, Mancilla-David F, Ellis K, Muljadi E, Jenkins P. A cell-to-module-to-array detailed model for photovoltaic panels. Solar Energy 2012;86(9):2695–706.
[45] K. solar, Kyocera (210W) KD210GX-LP Solar Panel. URL:http://www.buildsite.com/pdf/kyocera/KD210GX-LP-Product-Data-381922.pdf [accessed 08.12.2016].
[46] L.C.P. Inc. 5kWh Air Cooled Technical Manual, Product Manual; 2013.
[47] Solouk A, Shakiba-herfeh M, Kannan K, Solmaz H, Dice P, Bidarvatan M, Kondipati N, Shahbakhti M. Fuel economy benefits of integrating a multi-mode low temperature combustion (LTC) engine in a series extended range electric powertrain. SAE Technical Paper 2016-01-2361.
[48] ENOGIA SAS. Datasheet: ENOGIA's ENO-10LT ORC System Fact Sheet. URL:http://www.enogia.com/images/offer/datasheet-ENO10LT.pdf [accessed 06.07.2017].
[49] Razmara M, Maasoumy M, Shahbakhti M, Robinett III RD. Optimal exergy control of building HVAC system. J Appl Energy 2015;156:555–65.
[50] Razmara M, Bharati GR, Shahbakhti M, Paudyal S, Robinett RD. Bilevel optimization framework for smart building-to-grid systems. IEEE Trans Smart Grid 2018;9(2):582–93.
[51] Wang R, Xu Z, Pan Q, Du S, Xia Z. Solar driven air conditioning and refrigeration systems corresponding to various heating source temperatures. Appl Energy 2016;169:846–56.

[52] Jafari M, Gauchia A, Zhang K, Gauchia L. Simulation and analysis of the effect of real-world driving styles in an EV battery performance and aging. IEEE Trans Transp Electrification 2015;1(4):391–401.
[53] MISO. Midcontinent independent system operator. URL:https://www.misoenergy.org/ [accessed 18.09.2018].
[54] Lofberg J. YALMIP: a toolbox for modeling and optimization in MATLAB. 2004 IEEE international symposium on computer aided control systems design. IEEE; 2004. p. 284–9.
[55] Wächter A, Biegler LT. On the implementation of an interior-point filter line-search algorithm for large-scale nonlinear programming. Math Program 2006;106(1):25–57.
[56] G. Optimization Inc. Gurobi optimizer reference manual, 2015. URL:http://www.gurobi.com; 2014.
[57] Intellovations, LLC. Weather forecast accuracy details for Hancock, Michigan. URL:http://forecastadvisor.com/detail/Michigan/Houghton/49931/ [accessed 26.05.2018].
[58] Shahidehpour M, Yamin H, Li Z. Market operations in electric power systems: forecasting, scheduling, and risk management. John Wiley & Sons; 2003.
[59] Wang F, Mi Z, Su S, Zhao H. Short-term solar irradiance forecasting model based on artificial neural network using statistical feature parameters. Energies 2012;5(5):1355–70.